remote sensing

MDPI

Article

Optimized Parameters for Detecting Multiple Forest Disturbance and Recovery Events and Spatiotemporal Patterns in Fast-Regrowing Southern China

Yuwei Tu [1,2], Kaiping Liao [3], Yuxuan Chen [1,2], Hongbo Jiao [4] and Guangsheng Chen [1,2,*]

[1] State Key Laboratory of Subtropical Silviculture, Zhejiang A&F University, Hangzhou 311300, China; tyuwei@stu.zafu.edu.cn (Y.T.); chenyuxuan@stu.zafu.edu.cn (Y.C.)
[2] College of Environmental and Resource Sciences, Zhejiang A&F University, Hangzhou 311300, China
[3] Wudoujiang National Wetland Park Management Bureau, Ji'an 343900, China; sclysdb@163.com
[4] Forestry Industry Development Administration, Xinyu 338000, China; xycyhgk@163.com
* Correspondence: chengu1@zafu.edu.cn

Abstract: The timing, location, intensity, and drivers of forest disturbance and recovery are crucial for developing effective management strategies and policies for forest conservation and ecosystem resilience. Although many algorithms and improvement methods have been developed, it is still difficult to guarantee the detection accuracy for forest disturbance and recovery patterns in southern China due to the complex climate and topography, faster forest recovery after disturbance, and the low availability of noise-free Landsat images. Here, we improved the LandTrendr parameters for different provinces to detect forest disturbances and recovery trajectories based on the LandTrendr change detection algorithm and time-series Landsat images on the GEE platform, and then applied the secondary random forest classifier to classify the forest disturbance and recovery patterns in southern China during 1990–2020. The accuracy evaluation indicated that our approach and improved parameters of the LandTrendr algorithm can increase the detection accuracy for both the spatiotemporal patterns and multiple events of forest disturbance and recovery, with an overall accuracy greater than 86% and a Kappa coefficient greater than 0.91 for different provinces. The total forest loss area was 1.54×10^5 km^2 during 1990–2020 (4931 km^2/year); however, most of these disturbed forests were recovered and only 6.39×10^4 km^2 was a net loss area (converted to other land cover types). The area with two or more times of disturbance events accounted for 11.50% of the total forest loss area. The total forest gain area (including gain after loss and the afforestation area) was 5.44×10^5 km^2, among which, the forest gain area after loss was 8.94×10^4 km^2, and the net gain area from afforestation was 4.55×10^5 km^2. The timing of the implementation of forestry policies significantly affected the interannual variations in forest disturbance and recovery, with large variations among different provinces. The detected forest loss and gain area was further compared against with inventory and other geospatial products, and proved the effectiveness of our method. Our study suggests that parameter optimization in the LandTrendr algorithm could greatly increase the accuracy for detecting the multiple and lower rate disturbance/recovery events in the fast-regrowing forested areas. Our findings also offer a long-term, moderate spatial resolution, and precise forest dynamic data for achieving sustainable forest management and the carbon neutrality goal in southern China.

Keywords: forest disturbance; forest recovery; LandTrendr; parameter optimization; southern China

Citation: Tu, Y.; Liao, K.; Chen, Y.; Jiao, H.; Chen, G. Optimized Parameters for Detecting Multiple Forest Disturbance and Recovery Events and Spatiotemporal Patterns in Fast-Regrowing Southern China. *Remote Sens.* **2024**, *16*, 2240. https://doi.org/10.3390/rs16122240

Academic Editors: Nicola Genzano, Carolina Filizzola, Francesco Marchese and Valerio Tramutoli

Received: 29 April 2024
Revised: 17 June 2024
Accepted: 18 June 2024
Published: 20 June 2024

1. Introduction

Forest dynamic changes not only directly affect the global carbon cycle and carbon sequestration process, but also have important and far-reaching implications for both human and biosphere conditions [1,2]. Forest disturbances and recovery are the major causes of forest dynamics, which can be driven by many natural and anthropogenic factors

such as fire, windthrow, drought, heatwaves, biotic outbreaks, and harvest [3]. According to the 2023 Global Ecological Environment Observation Analysis Research Cooperation (GEOARC), the total global forest loss area was 582.17 Mha, and the total forest gain area was 342.16 Mha during 1985–2020. The global forest loss and gain rate has shown a significant acceleration trend during the past several decades [4,5]. Therefore, the timing, location, intensity, and drivers of forest disturbance and recovery are crucial for understanding the dynamic changes of forest structure and functions and developing effective management strategies and policies for forest conservation and ecosystem resilience [6–8].

The free availability of the United States Geological Survey (USGS) has catalyzed Landsat time-series analysis for forest change detection [4]. Unlike the traditional method of visually interpreting dual-temporal or multi-temporal satellite images to determine forest disturbance and recovery [9,10], Landsat time-series analysis can be used to more accurately track changes in forests, and even identify multiple disturbances that have occurred over a period of time [11,12]. Based on Landsat images, many automated analysis algorithms have been developed, such as a Vegetation Change Tracker (VCT) [13], Breaks For Additive Season and Trend (BFAST) [14], Exponentially Weighted Moving Average Change Detection (EWMACD) [15], Continuous Change Detection and Classification (CCDC) [16], and Landsat-based detection of Trends in Disturbance and Recovery (LandTrendr) [17], among which, the LandTrendr is the most widely-used annual-scale algorithm in detecting forest disturbance and recovery. Some studies have also compared the difference and advantage of these algorithms, and identified the best algorithm at different application regions [18,19]. For example, Ding and Li [19] compared the performance of VCT, LandTrendr, BFAST, and CCDC in detecting forest disturbances in a region of southeastern China, and concluded that the LandTrendr algorithm performed the best and was more suitable for forest disturbance detection in this region. The LandTrendr algorithm has also evolved from a single input variable [17,20] to eight or more variables [21,22], and from LandTrendr only to integrated LandTrendr and the random forest (RF) method [22,23]. The secondary classification method of RF can effectively synthesize the advantages of multiple vegetation indices (VIs) and other assisting factors, and constrains the detected disturbance and recovery patterns using the observational plot data. Thus, this can help avoid the possible noises caused by a single VI, such as the most commonly used NBR (Normalized Burn Ratio) [22,23].

In addition, some studies have also tried to improve the LandTrendr performance to detect forest disturbance and recovery. For example, Qiu et al. [24] modified the LandTrendr algorithm (mLandTrendr) by combining multiple VIs and multi-season indices and improving the Savitzky–Golay (SG) filtering method. Their results indicated that the detection accuracy increased by 21%. However, fewer studies have paid attention to calibrating the LandTrendr parameters, which could affect the fitting trajectories of various VIs and the identification of vertices [24]. And eventually, these parameter settings will affect the detection accuracy for exact disturbance timing and multiple disturbance events. Most studies chose the default parameters in the LandTrendr algorithm when applying the LandTrendr algorithm for forest disturbance and recovery detection in different regions [25,26]. As suggested in Kennedy et al. [17], the parameter values could vary in a wide range and greatly affect the detection accuracy. For example, the max segment parameter in LandTrender can control the number of recognized disturbance events, and the setting range of this parameter generally varies from 4 to 10. In addition, the Recovery Threshold parameter can vary between 0.25 and 1.0 [24], representing that the minimum recognized recovery year is 1/Recovery Threshold, which could cause a failure to identify the disturbance events when the recovery time is less than 1/Recovery Threshold. Several studies have suggested that the LandTrendr parameters should be optimized for better detection accuracy. For example, de Jong et al. [26] detected the mangrove dynamic and compared the effects of the Max Segment, Recovery Threshold, and Best Model Proportion on the detection accuracy using LandTrendr. Liu et al. [25] compared the performance of different Max Segment and Recovery Threshold values on the detection of fire disturbance and recovery in Australia.

However, it is still unclear how the recovery rate of trees affected the effectiveness of LandTrendr parameters in detecting forest disturbances.

Southern China is mainly located in the subtropical and tropical climate zone. The warm and wet climate in this region leads to a fast recovery of the forest canopy after a disturbance, especially in the most southern provinces such as the Guangxi and Guangdong Province. In addition, southern China is now the main timberland base in China and a large area of fast-growing forest plantations (rotation age is 5–14 years) are planted, such as the Eucalyptus and poplar trees. For example, the Eucalyptus area accounts for about 20.4% and 14.6% of total forest area in the Guangxi and Guangdong Provinces, respectively. The Guangxi Province solely produced about 38.6% of the timber supply of the entirety of China in 2021. The fast rotations of forests could result in multiple forest disturbance and recovery events in a short period. Furthermore, most of the VIs used in the LandTrendr such as NBR, NDVI, and TCG (Tasseled Cap Greenness) only reflect the canopy changes of reflectance, so the fast recovery of the forest canopy in southern China could easily result in the failed identifications of the actual disturbance and recovery years, especially when the availability of noise-free Landsat images is low in this high-cloud-cover and high-rainfall region. Except for the above-mentioned improvements in the Landsat image quality, the SG filtering method, as well as multi-season and multi-VI integrations, a cautious calibration of the LandTrendr parameter values will exert magnified effects on reducing the detection uncertainties of forest disturbance and recovery patterns caused by the complex climate, topography, forest types, and low availability of noise-free Landsat images in southern China.

In this study, we targeted the optimization of the LandTrendr parameters to increase the detection accuracy of forest disturbance and recovery events in fast-recovering southern China, and further ran the LandTrendr to classify their spatiotemporal patterns. The specific objectives are to (1) identify the most sensitive parameters and calibrate their values in LandTrendr algorithms, and assess the accuracy of improved parameter values in identifying forest disturbances and recovery in southern China; (2) classify the forest disturbance and recovery patterns by combining the LandTrendr algorithm and RF classifier on the GEE platform; and (3) analyze the spatiotemporal patterns in forest disturbances and recovery. This study can provide an improved LandTrendr parameter sets for forest disturbance and recovery detection and an accurate forest dynamic dataset for forest management and policy making in southern China.

2. Study Area and Data

2.1. The Study Region

The research area is located in southern China, including seven provinces and one municipal city: the Yunnan Province, Guizhou Province, Sichuan Province, Chongqing City, Hunan Province, Guangdong Province, Guangxi Province, and Fujian Province (Figure 1). To be convenient, Chongqing City is combined in the Sichuan Province for analysis in this study (we only mention seven provinces thereafter), since Chongqing belonged to Sichuan Province before 1997 (there are no statistical data before this time). The entire study area spans about 24° longitude, with large differences in the vegetation coverage, terrain, climate, and hydrology. This region has diverse terrain types, including mountains, hills, and plains, and is one of the most ecologically diverse and forest-rich regions in China, covering a vast geographical range in the subtropical zone of China. This region has a relatively warm and humid climate. The annual average temperature varies between 15 and 22 °C. The annual average precipitation gradually increases from the west to the east, with the annual precipitation exceeding 900 mm in most areas.

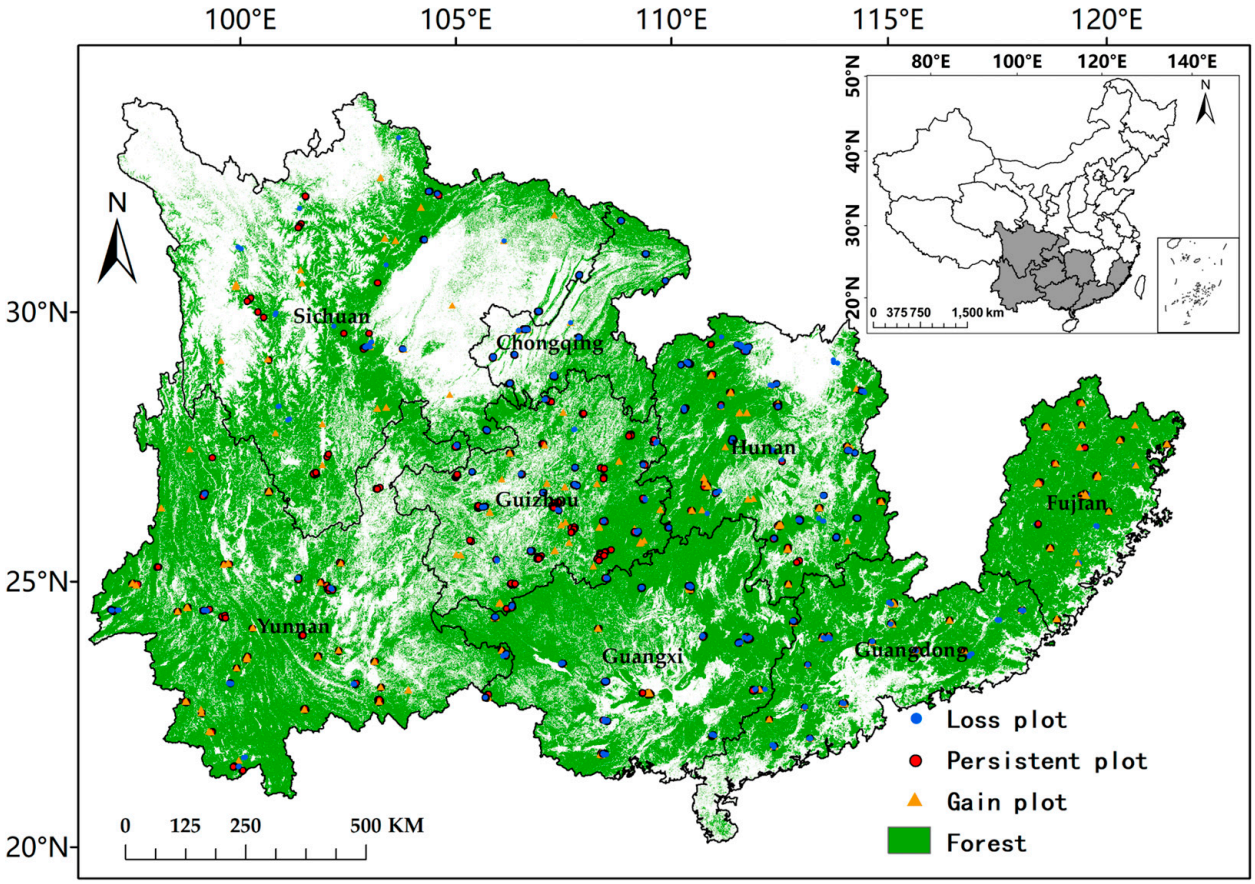

Figure 1. The locations of the study area, provinces, and the sampling plots representing persistent forest, forest gain, forest loss, and non-forest areas.

The forest coverage is about 50% for this study region, and the total forest area accounts for approximately 39% of the national forest area. The forest types mainly include subtropical evergreen broadleaf, evergreen needleleaf, and mixed broadleaf and needleleaf forests, as well as a small portion of tropical broadleaf rainforests. Due to natural disasters, population growth, economic development, agricultural expansion, and other human activities, forest disturbances frequently occurred in this region and the disturbance regimes are complicated. Meanwhile, different provinces have also implemented a series of forestry policies and regulations to protect and restore forest resources, such as the Natural Forest Protection Program (NFPP), the Grain for Green Program (GFGP), the Mid-Upper Reaches of the Yangtze River Shelterbelt Project, the Pearl River Shelterbelt Project, and the Coastal Shelterbelt Project.

2.2. The Work Flow

The work flow of this study is summarized in Figure 2 and described in detail in the below sections. Due to fewer available Landsat images before 1990, our study focused on the 1990–2020 period. Due to there being less accuracy in detecting small fractional disturbances at a grid scale for the LandTrendr algorithms, we only detected the stand-replacing (i.e., >70% tree loss at a 30 m × 30 m pixel) forest disturbance and recovery.

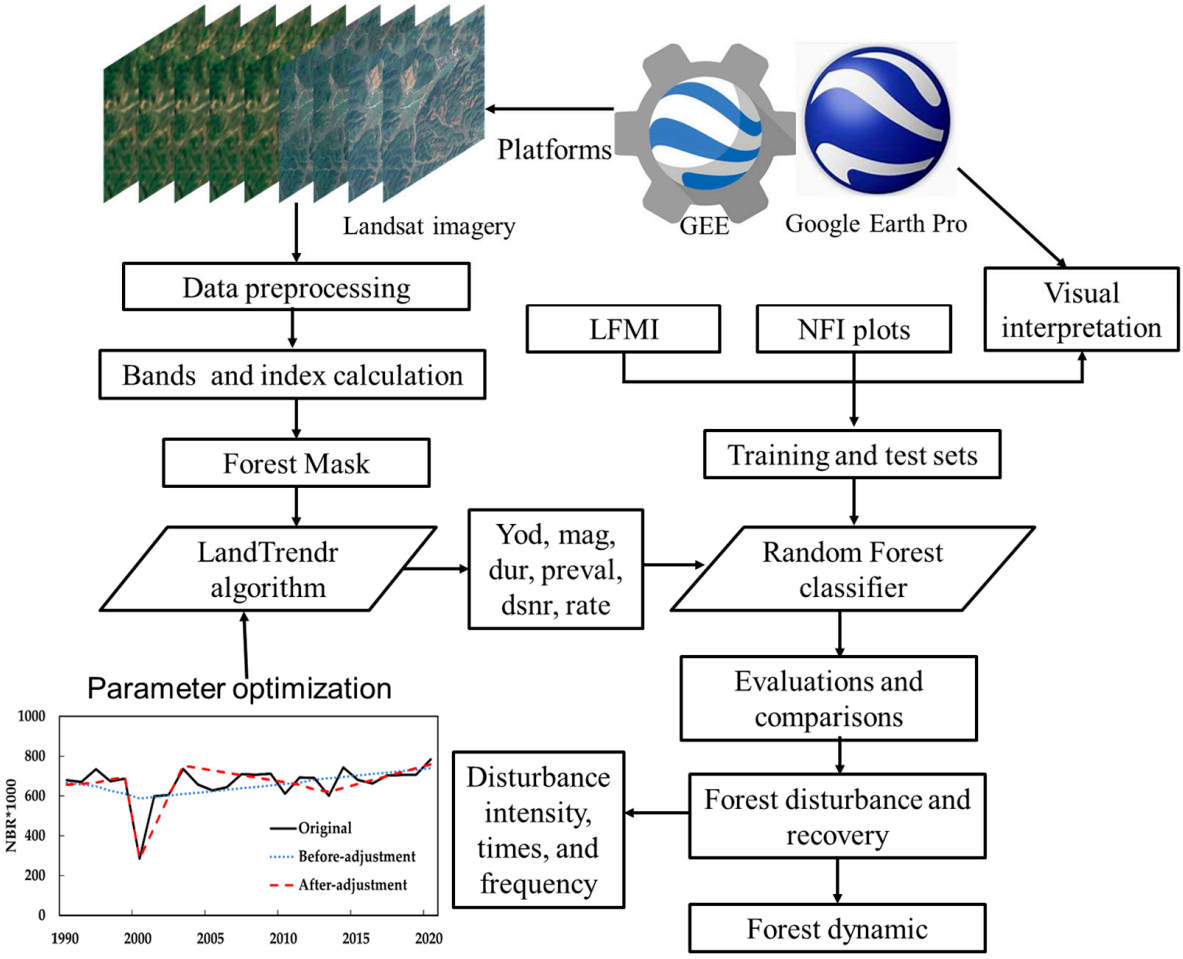

Figure 2. The work flow of this study. Note: NFI: national forest inventory; LFMI: local forest management inventory; GEE: Google Earth Engine.

2.3. The Time-Series Landsat Images and Preprocessing

The acquisition and processing of remote sensing images and the operation of algorithms were conducted on the GEE platform (https://earthengine.google.com/, accessed on 16 April 2024), covering the time range from 1990 to 2020. The collected data were the surface reflectivity of Landsat5 TM, Landsat7 ETM+, and Landsat8 OLI sensors. The LEDAPS algorithm was used for atmospheric correction for Landsat5 TM and Landsat7 ETM+ data, and the LaSRC algorithm was used for Landsat8 OLI data. Considering the impact of phenological changes on forest disturbance detection, this study selected all available images during the growing season from June to September. A total of 5537 scenes of Landsat images were included in this study. After a series of preprocessing steps, including cloud masking, shadow removal, stitching, and cropping, we generated a mosaicked image for each year, and built a reliable time-series image stack. For each image, the six bands of Landsat data (Blue, Green, Red, Near Infrared, Shortwave Infrared 1, and Shortwave Infrared 2) were used to compute the multiple VIs.

2.4. Training and Test Sampling Plot Data

To evaluate the performance of the forest mask for the study region, we used the all-season sample set data developed by the Finer-Resolution Observation and Monitoring of Global Land Cover (FROM-GLC) project [27]. In total, 4268 training plots and 1757 validation plots were included.

For training and evaluating the detection of forest disturbance and recovery, we collected sampling plot data from three sources including local forest management inventory

(LFMI) plots, NFI (National Forest Inventory) plots, and the visual interpretation plots based on the high-resolution satellite images from the Google Earth Pro platform. For the LFMI, we have the forest watershed data from three counties in the Guizhou Province, and we identified 105 plots from these counties. For the NFI, we have the fourth NFI (1989–1993) plot data and a total of 310 plots (178 records with forest disturbances and the rest are non-forest plots). For the visual interpretation, we first used the LandTrendr-calculated NBR trajectory data to preliminarily determine the year of forest disturbance/recovery occurrence. And then, we identified the actual forest disturbance plots based on the high-resolution (<5 m) images (e.g., aerial photos, Quickbird, IKONOS, and SPOT images) on Google Earth Pro. At least two images spanning less than 5 years (due to a lack of enough high-resolution images) before and after forest disturbance were selected to confirm the occurrence timing of the disturbance. The plots were chosen at the areas with tree loss > 70% (standing-replacing disturbance) and with a loss area greater than 30 m × 30 m (bigger than a pixel). Three types of sampling plots were divided, including forest loss, forest gain, and persistent (no change) forest plots. A total of 3590 sample plots were generated, including 871 forest loss plots, 884 forest recovery plots, and 1835 persistent forest plots (Figure 1). In total, 70% plots were used for training the RF method and the rest of the plots, the other 30%, were used for validation.

2.5. Forest Distribution Area Mask

To reduce the impact of non-forest areas such as farmland and grassland on forest disturbance and recovery monitoring, a forest mask was generally first developed before running the LandTrendr change detection algorithm. We collected the 1990–2020 China Land Cover Datasets (CLCD) [28], covering eight periods (1980s, 1990, 1995, 2000, 2005, 2010, 2015, and 2018) of national land cover datasets (NLCD) [29] at a spatial resolution of 30 m and the 2017 land cover data at a 10 m resolution (FROM-GLC10) [30]. The FROM-GLC10 data were further aggregated to a 30 m spatial resolution and reclassified into forest and non-forest covers. The maximum extent of the forest distribution area was generated by including all pixels with forest distribution in all above datasets during 1990–2020. The statistical forest area (95.1×10^4 km^2) based on the ninth NFI (2014–2018) was further used to constrain the total forest area in 2020 and ensure that the forest area is accurate. Based on the FROM-GLC training and validation plots, we assessed the overall accuracy of the developed forest mask data. The overall accuracy was 0.91, which was precisely enough since this forest mask was just used for screening out the non-forest area.

3. Methods

3.1. LandTrendr Change Detection Algorithms

LandTrendr is an algorithm designed for analyzing time-series of remote sensing images, primarily employed in detecting surface changes, disturbances, and recovery trends [17,31], and can detect both slow and abrupt disturbance events, which may include forest fires, harvesting, land use changes, insects and diseases, and windthrow. The fundamental concept of this algorithm revolves around constructing a time-series dataset from multi-temporal remote sensing imagery and conducting time-series analysis on individual pixels. These time-series data are partitioned into a series of interconnected line segments, representing changes in surface reflectivity over time. Subsequently, LandTrendr algorithm applies regression analysis and curve fitting techniques to model the trend of each segment. Change detection is achieved by analyzing the slope and peak of time-series data. The specific processes include removing noise interference, identifying potential breakpoints, fitting spectral trajectories, simplifying, and selecting the best model. The more detailed mechanisms of LandTrendr algorithms are referred to in much of the previous literature [17].

The NBR is the most common VI used to detect forest disturbance and recovery in LandTrendr [22,23]. Due to the low availability of cloud-free scenes and frequent noises of Landsat images in the subtropical China, a single VI may result in the failure to detect all

disturbance events. Cohen et al. [22,23] found that the secondary classification combining various wave bands and spectral indices can effectively improve the accuracy of forest disturbance monitoring and effectively reduce the classification errors. Based on the initial running and comparisons of LandTrendr at sample plots, our study finally chose four bands and 5 VIs to detect forest disturbance and recovery. The VIs include NBR, Normalized Difference Moisture Index (NDMI), Tasseled Cap Brightness (TCB), Greenness (TCG), and Wetness (TCW). The bands include B2 (Green band), B4 (NIR; Near Infrared), and B5 (SWIR1; Short-wave Infrared Band 1). The outputs of LandTrendr were an array of datasets with six bands including yod (identified year of disturbance), mag (change magnitude of spectral values), dur (duration of a disturbance event), preval (pre-values of spectrum), dsnr (Detection Signal-to-Noise Ratio), and rate (rate of spectral change). These outputs were used as input variables for subsequent secondary classification.

3.2. LandTrendr Parameter Calibrations

All LandTrendr processes involved some parameters, which affects the fitting trajectories of various VIs and the identification of breakpoints. Therefore, it is necessary to recalibrate parameters to ensure the accuracy of LandTrendr change detection when applying at different regions. To optimize the parameters of LandTrendr, we first chose 20 plots with forest disturbance and recovery records from the sampling plots in each province (totaling 140 plots for the study region), then we ran LandTrendr at these locations with modified parameter values. Through evaluations using the sampling plot data, we determined the best parameter values. Finally, the calibrated parameter values are shown in Table 1. We found that Max Segments and Recovery Threshold were more sensitive. The analysis indicated that the changes of Max Segments and Recovery Threshold parameter values can increase the accuracy for detecting multiple disturbance events and fast-recovery plantation. Due to the fast rotation of forests in the study region, there were several times of disturbance for many areas during 1990–2020. When the max segment parameter increased from 4 to 8, the fitted segments increased and thus we can detect multiple disturbance events. In addition, due to the difference of disturbance extent and severity, many VIs could be recovered to pre-disturbance levels within 2–5 years. This phenomenon was particularly notable in Guangxi and Guangdong provinces due to the larger area of fast-growing Eucalyptus plantations (which generally rotate every 5–14 years) and relatively higher temperature and humidity levels [32]. Consequently, forest canopy recovery for many timberlands tended to be less than 4 years. If a segment has a recovery rate which is faster than 1/Recovery Threshold (in years), then the segment is not considered as disturbance. This means that the forest disturbance events that recover in a time shorter than 4 years will not be detected if the Recovery Threshold is set as 0.25. Therefore, the Recovery Threshold was adjusted from 0.25 to 0.5 for Guangxi and Guangdong provinces.

Table 1. Calibrated parameters and values for the LandTrendr algorithm.

Parameter	Parameter Description	Ranges	Default Value	Optimized Value
Max Segments	Maximum number of segments to be fitted on the time-series	4–10	10	8
Spike Threshold	To attenuate peaks or outliers in the pixel value trajectory, if the percentage difference between the values of two adjacent time points is less than that value, the value will be considered an outlier and needs to be eliminated	0.75–1.0	0.9	0.9
Vertex Count Over Shoot	The number of nodes that can be exceeded in the regression of potential nodes in the initial stage	0–3	3	3

Table 1. *Cont.*

Parameter	Parameter Description	Ranges	Default Value	Optimized Value
Recovery Threshold	If a segment has a recovery rate faster than 1/Recovery Threshold (in years), then the segment is not considered as disturbance	0.25–1.0	1.0	0.5 (Guangxi, Guangdong) 0.25 (the rest)
Pval Threshold	If the *p*-value of the fitted model exceeds this threshold, then the current model is discarded and another is fitted using the optimizer	0.05, 0.1, 0.2	0.05	0.05
Best Model Proportion	Takes the model with most vertices that has a *p*-value that is at most this proportion away from the model with lowest *p*-value	0.5–1.2	0.75	0.75
Change Magnitude Threshold for stand-replacing loss	The minimum change magnitudes used to remove the persistent forest pixels before running the RF method	0–1000	-	200–280

3.3. Secondary Classification Using the RF Classifier

Cohen et al. [22,23] found that the detection accuracy of forest disturbance and recovery can be improved by performing secondary classification through a two-level classification model, allowing it to effectively utilize different bands and spectral indices. The RF classifier was generally used to perform secondary classification on the results obtained from the single-band or single-index LandTrendr algorithm. RF is a machine learning method based on ensemble learning. It builds multiple decision trees to perform classification or regression tasks. The advantages of the RF algorithm are its good adaptability to high-dimensional data and large-scale datasets, the ability to handle multi-class classification problems, good robustness, less influences from noise and outliers, and less prone to overfitting [33]. It usually does not require complex parameter adjustment. Except for the yod band (the year of disturbance), another five bands of LandTrendr outputs including mag, dur, rate, dsnr, and preval were integrated into an image stack and used as the input features for RF. Therefore, a total of 40 variables (5 outputs × 8 spectral indices) were used.

All sampling plots were used to either train or validate the RF classifier, in which 70% (2513 plots) were randomly selected for training, and 30% (1077 plots) were used for validation. The number of decision trees is an important parameter that directly affects the performance and behavior of the RF model. Too few decision trees may lead to underfitting, which cannot capture the complex relationships in the data. If the tree number is too large, it may lead to overfitting, resulting in good performance on the training data, but poor classification performance. In this study, cross-validation was applied on GEE to explore the influence of the number of different decision trees on the model performance, and we found that the optimal number of selected decision trees was 35 when the model accuracy reached 93.8%.

We further calculated the relative importance of input variables in the RF model after modifying the number of decision trees. We found that the contributions of variables varied in different provinces. For example, the change rate of TCW and B2 (Green band) and NBR magnitude had the highest importance for Guangxi Province. The magnitudes of NBR and NDMI had the highest importance for Sichuan Province (Figure A1; only showing the top 10 variables). The NIR magnitude and dsnr of NDMI were the most important for Fujian Province. The magnitude and prevalue of NDMI were the most important for Guangdong Province. The magnitudes of NDMI and NBR, as well as NDMI change rate were the most important for Yunnan Province. These suggested that the major contributing factors for various provinces were different due to the difference in climate, vegetation cover, topography, and disturbance regimes.

3.4. Accuracy Assessment

The 2513 sample plots for validation were used to evaluate the detection accuracy. We first chose the evaluation metrics of overall accuracy (OA), user accuracy (UA), producer accuracy (PA), and Kappa coefficient. These metrics collectively offered a comprehensive evaluation of diverse facets of the model's performance [34]. The overall accuracy metric encapsulated the model's overall classification precision, while user accuracy and producer accuracy scrutinized the model's precision in classifying specific categories and its proficiency in capturing samples of particular categories, respectively. The Kappa coefficient measured the agreement between the model's classification outcomes and random classification, thereby enabling a more holistic appraisal of the model's performance [34]. In addition, we also chose 5 sites with available high-resolution images and disturbance occurrence to visually compare the consistency between images and our detected results and between the global forest change (GFC) disturbance product [4] and our results. The GFC product during 2001–2023 has an OA greater than 80% for disturbance area detection.

To quantitatively evaluate the performance of forest disturbance and recovery detection at spatial scale, we also conducted the Intersection over Union (IoU) analysis. IoU analysis is a commonly used metric for evaluating the performance of object detection models. It assesses the accuracy of detection results by comparing the intersection and union of predicted bounding boxes with ground truth bounding boxes. Mathematically, the IoU calculation formula is:

$$\text{IoU} = \frac{\text{Intersection}}{\text{Union}} \quad (1)$$

Here, Intersection denotes the matched grid numbers between predicted and observed results, and Union denotes all the grid numbers of both predicted and observed results.

We randomly selected an area with available high-spatial-resolution (<5 m) images on the GEE platform, and then we digitized the boundary of forest loss area (observed disturbance area). Then our detected forest disturbance product was overlaid and compared with the observed disturbance area to calculate the Intersection and Union grid cell numbers, and finally the IoU was calculated by following Equation (1).

3.5. Analysis Methods

Based on the classified annual disturbance and recovery data, we further calculated the disturbance times (frequency) within each pixel during the study period. To more clearly present the disturbance patterns, the 30 m forest disturbance and recovery data were further converted to 10 km using the aggregation method, which represented the disturbance severity. A sensitivity and uncertainty analysis for the detected forest loss and gain area was conducted by tuning the most sensitive Max Segment and Recovery Threshold parameters. We applied the similar approaches and parameter value ranges in Liu et al. [25] to do the sensitivity and uncertainty analyses. A rectangular region with 50 km^2 from each province was selected at the areas with denser sampling plots. The combined changes of Max Segment (4, 6, 8, 10, and 12) and Recovery Threshold (0.25, 0.5, 0.72, and 1.0) were applied, and in total, 20 LandTrendr simulation experiments based on NBR were run. The standard deviations (δ) were further calculated based on the 95% confidence interval, and the uncertainty ranges owing to parameters were represented by mean values $\pm 2\delta$.

The GEE platform, Microsoft excel, SPSS 20.0 (SPSS Inc., Chicago, IL, USA), and ArcGIS 10.8 software were applied to process data, draw figures and maps, and conduct statistical analyses.

4. Result

4.1. Accuracy Assessment

The accuracy assessment results using the validation sampling plots indicated that the optimized LandTrendr parameters and the combination of the LandTrendr algorithm and

the RF secondary classification can improve the accuracy of forest disturbance and recovery monitoring. For the detection of forest loss, the overall accuracies were all greater than 91%, and the Kappa coefficients were all higher than 0.86 for all provinces (Table 2). For the detection of forest recovery, the overall accuracies were all greater than 93%, and the Kappa coefficients were higher than 0.88 for all provinces (Table 3). The highest accuracy in the Guizhou Province was because this province has fewer human impacts on forests and thus has fewer disturbance events. In addition, this province has mostly mountainous terrains and thus the boundary between forest and other land cover types can be easily separated, which reduces the classification errors for land cover changes. These demonstrated that our method can effectively capture the stand-replacing forest disturbance and recovery area in terms of the sampling plot data.

Table 2. Accuracy assessment for detected forest loss area. OA1 and Kappa: overall accuracy and Kappa coefficients based on optimized parameters; OA2: overall accuracy based on default parameters.

Regions	Producer Accuracy	User Accuracy	OA1	Kappa	OA2	OA Change (%)
Hunan	95%	93%	95%	0.89	87%	9.20
Yunnan	91%	94%	91%	0.88	89%	2.25
Guizhou	97%	97%	97%	0.94	89%	8.99
Guangdong	93%	91%	92%	0.88	86%	6.98
Sichuan	97%	92%	95%	0.89	87%	9.20
Fujian	90%	95%	92%	0.91	89%	3.37
Guangxi	89%	95%	92%	0.86	85%	8.24

Table 3. Accuracy assessment for detected forest gain area.

Province	Producers Accuracy	User Accuracy	Overall Accuracy	Kappa
Hunan	98%	92%	94%	0.88
Yunnan	97%	92%	95%	0.90
Guizhou	98%	93%	96%	0.93
Guangdong	95%	92%	93%	0.89
Sichuan	97%	96%	97%	0.94
Fujian	97%	95%	96%	0.92
Guangxi	92%	98%	95%	0.89

To further evaluate the performance of the classification at a spatial scale, we randomly selected five scenes of high-resolution images from Google Earth Pro and visually digitized the forest loss boundaries (Figure 3). For most scenes, our detected forest loss boundary matched well with the visually-interpreted loss polygons, and were also generally consistent with the GFC-classified forest loss area at a spatial scale; however, for the locations with lower rates of forest loss (i.e., about 70% tree loss), the GFC product failed to capture the actual forest loss areas (e.g., Figure 3a). This suggested that our combined method and improved parameters can more accurately detect the spatiotemporal patterns of forest disturbance.

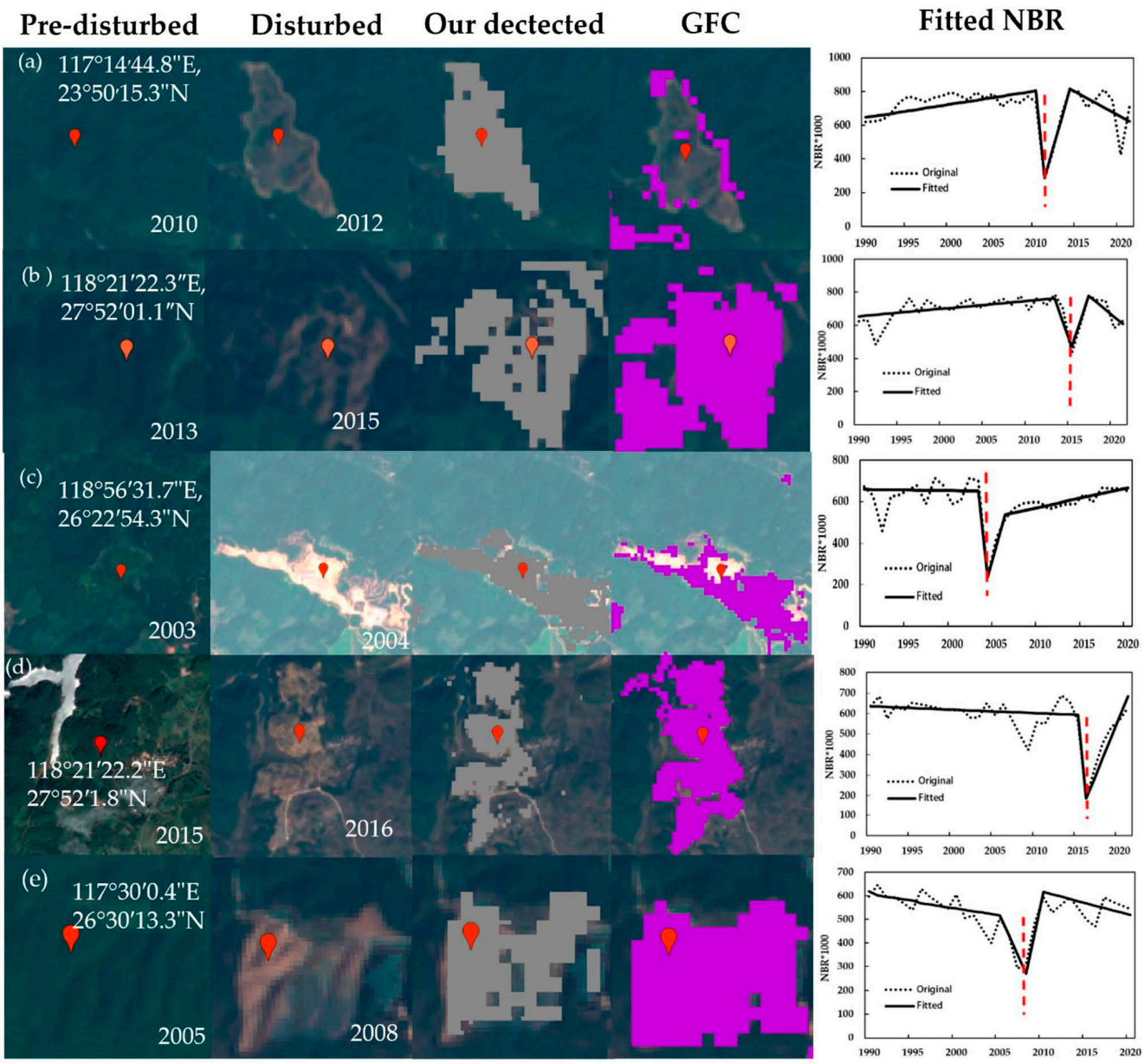

Figure 3. Comparison of classified forest loss/gain area with the visually interpreted loss/gain area and GFC forest loss product based on NBR at five locations (**a**–**e**) with available high-resolution images. Note: GFC is the global forest change product [4]. The red dashed line is the identified disturbance year based on the fitted trajectory of Normalized Burned Ratio (NBR).

The spatial consistency between our detected and observed disturbance area was conducted by randomly selecting an area for IOU analysis. The randomly selected area has experienced forest disturbances two times between 2015 and 2020 (Figure 4). Compared with the visually interpreted disturbance boundary, we found that the IoU of our classified results was 65.2%, while the IoU of the GFC product was 40.5%, indicating a better performance than the widely applied GFC product. The lower IoU rate was due to the mixed pixels with both disturbed and non-disturbed patches within a grid cell.

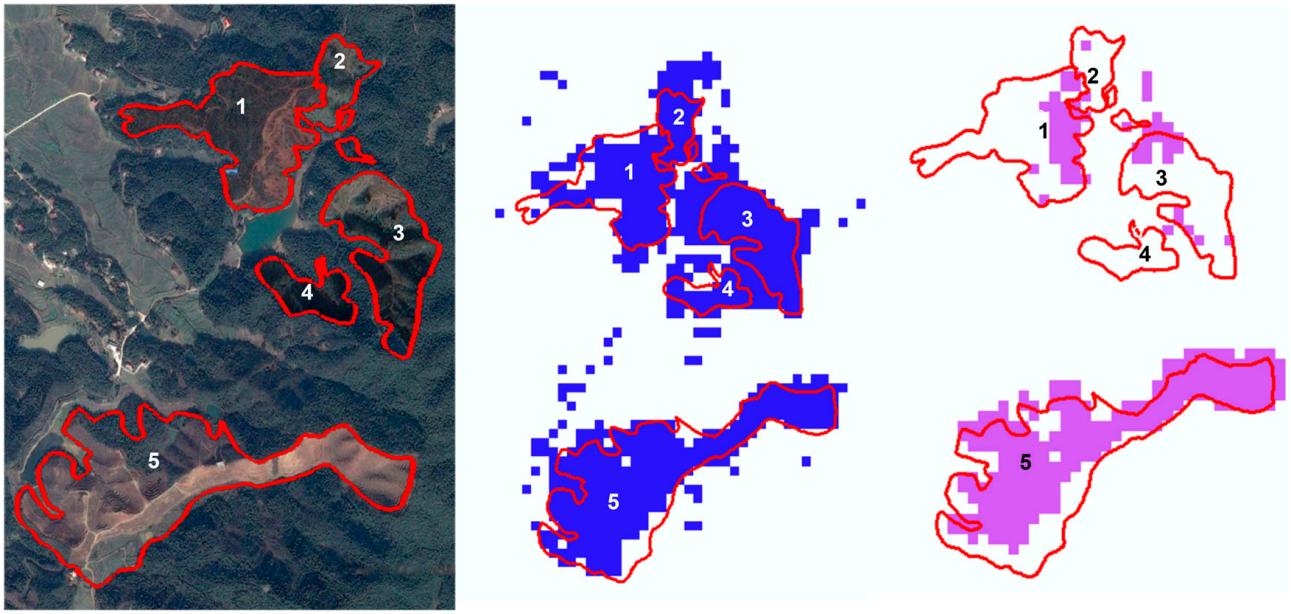

(**a**) (**b**) (**c**)

Figure 4. The selected area for IoU analysis in Taojiang County, Hunan Province, during 2015–2020. Note: (**a**): The manually digitized disturbed areas (loss year 2015: zones 1 and 4; 2017: zones 2, 3, and 5) based on the Google Earth Pro high-resolution images; (**b**): our classified disturbed areas; (**c**): disturbed area from the Global Forest Change (GFC) product.

4.2. The Effects of Optimized Parameters

A sensitivity analysis was conducted for the detected forest loss and gain area using the different parameter values of the Max Segment and Recovery Threshold. The results indicated that the changes of two parameters can significantly affect the detected forest loss and gain area (Tables A1 and A2). The identified pixel numbers for both the forest loss and gain area generally increased with the increasing parameter values of the Max Segment and Recovery Threshold. The maximum difference in the disturbance pixel numbers can be over 6 and 30 times for the forest loss and gain area, respectively. The identified pixel numbers using the optimized parameter values were at the lower range of the detected loss and gain area. These suggested that parameter calibration is very important for improving the accuracy of forest disturbance and recovery detection in southern China.

To further look at the effects of changing parameter values, we conducted a comparison at a plot level. The results indicated that the optimized parameters can more accurately detect the smaller fractional loss and multiple loss events (Figure 5). From Figure 5a,c, the refitted NBR curves can detect the fast (<3 years) canopy recovery disturbance events, while the fitted trajectories using default parameters failed to identify this disturbance event. From Figure 5b, the refitted curves can identify two consecutive stand-replacing disturbance events spanning 7 years, indicating an increased performance to detect the multiple disturbance events within a short period. From Figure 5d, the lower-rate disturbance events can also be detected based on the optimized parameters.

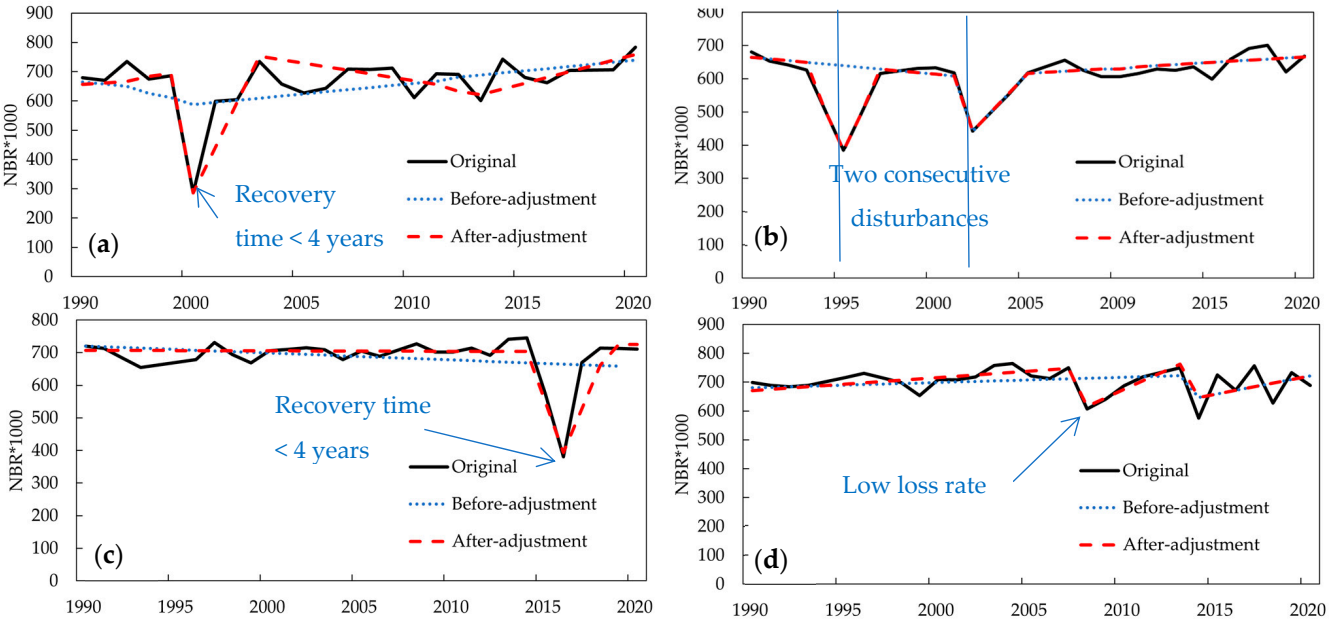

Figure 5. The LandTrendr identified breakpoints for disturbance events with the optimized and the default (original) parameter values at four randomly-selected sampling plots (**a**–**d**) based on the fitted NBR change magnitudes.

For the entire study region, the mean overall accuracy and Kappa coefficient increased by 6.89% and 3.65%, respectively, compared with the detection accuracy using the default parameters (Table 2). The higher increases of accuracy occurred in the Hunan and Sichun provinces, which have less forest loss area. The final detection accuracy was compounded by the RF secondary classification process; therefore, we further compared the LandTrendr results using the single NBR as an indicator (Figure 6). Using the Guangxi Province as an example, we found that the fraction of the forest loss area with two or more disturbance times before and after parameter optimization was 23.65% and 36.79%, respectively. The overall accuracy before and after parameter optimization was 57% and 76%, respectively. This indicated that parameter optimization can significantly increase the detection of multiple disturbance times and the overall accuracy. Notably, the overall accuracy using the single NBR was very low because the image quality was poor in southern China. The detected total forest loss area in the Guangxi Province during 1990–2020 was 10,488 and 55,002 km^2, respectively, which was either significantly lower or greater than the finally detected forest loss area (41,024 km^2) in Guangxi. This implied that there was large uncertainty in detecting forest disturbances in this region. In addition, it also suggested that NBR alone was not accurate enough to detect forest disturbances and it was necessary to apply the secondary classification method by combining multiple spectral bands or indices when applying the LandTrendr algorithm in this region.

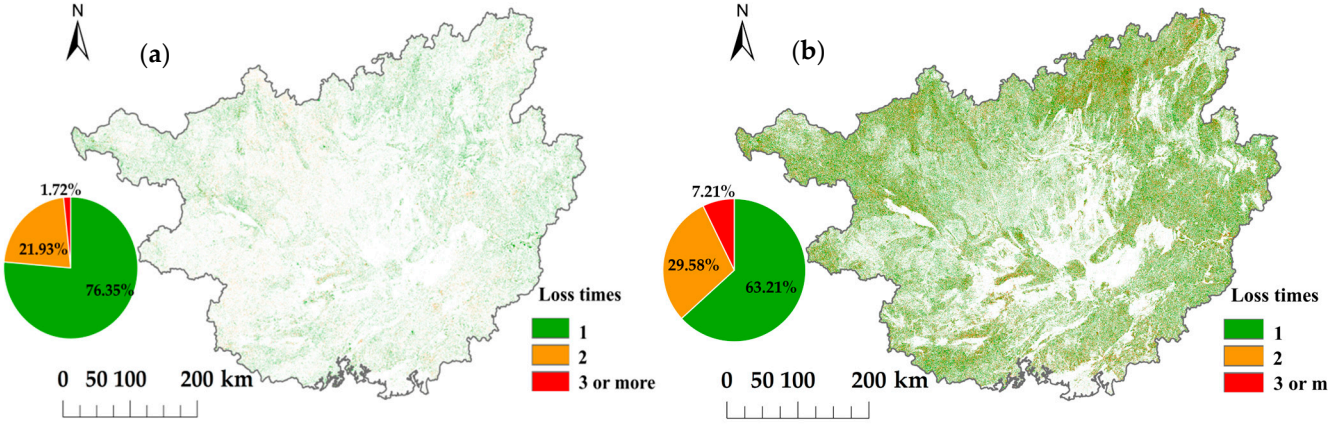

Figure 6. The comparison of the detected forest loss area and the fraction of disturbance times using default parameters (**a**) and optimized parameters (**b**) in Guangxi Province.

4.3. Spatiotemporal Patterns in Forest Loss Area

The total forest disturbance area including both temporary (e.g., loss due to harvest, fire, pest, and windthrow) and permanent (land use change) forest loss was 1.54×10^5 km^2 during 1990–2020, which accounted for 34.9% of the total forest area in 1990 (Figure 7). The mean annual loss area was $4.98 \times 10^3 \pm 1.15$ km^2. The mean coefficient of variation (CV) was 23.12% due to the variations of the Max Segment from 4 to 10 and the Recovery Threshold from 0.25 to 1.0. This implied that the parameter calibration is very important to increase the detection accuracy. The greatest and smallest loss area occurred in 1992 (9882 km^2) and 2001 (2697 km^2), respectively. The forest loss area showed a decline from 1990–1992 and a significant increasing trend (slope = 69.5 km^2/year) from 1993 to 2020, though the interannual variations in the loss area were very large (Figure 7).

At provincial levels, the Guangxi and Guangdong Provinces had the greatest loss areas of 4.10×10^4 km^2 and 3.46×10^4 km^2, respectively, while the Guizhou and Hunan Provinces had the smallest loss areas of 0.61×10^4 km^2 and 1.22×10^4 km^2, respectively (Figure 7). The loss rates relative to the forest area in 1990 were the highest in Guangxi (78.5%) and Guangdong (71.1%) and the smallest in Sichuan (13.0%) and Hunan (18.1%). All provinces showed the largest forest loss area in 1992. The Guizhou, Guangxi, Hunan, and Sichuan Provinces showed significant increasing trends of 14.7 km^2/year, 40.5 km^2/year, 9.9 km^2/year, and 11.3 km^2/year, respectively, during 1993–2020, with more obvious increasing trends since 2000, while other provinces showed no significant changing trends during 1993–2020.

On a spatial scale, most of the lost forest areas were located in the southern provinces of Guangxi, Fujian, and the Guangdong Province, and a concentrated loss area was found in the central Sichuan Province (Figure 8). From the magnified areas, we can more clearly see that the forest loss area of each year was mainly concentrated as many clustered patches since the main stand-replacing disturbance type in this region is harvesting. Forest loss severity is calculated by the fraction of the total loss area during 1990–2020, accounting for 2020's total forest area within each 10 km × 10 km pixel (Figure 9). The results indicated that the Guangxi, Guangdong, and Fujian Provinces had large areas with a disturbance severity higher than 80%, while a few areas in the Yunnan and Sichuan Provinces also had very high loss severity.

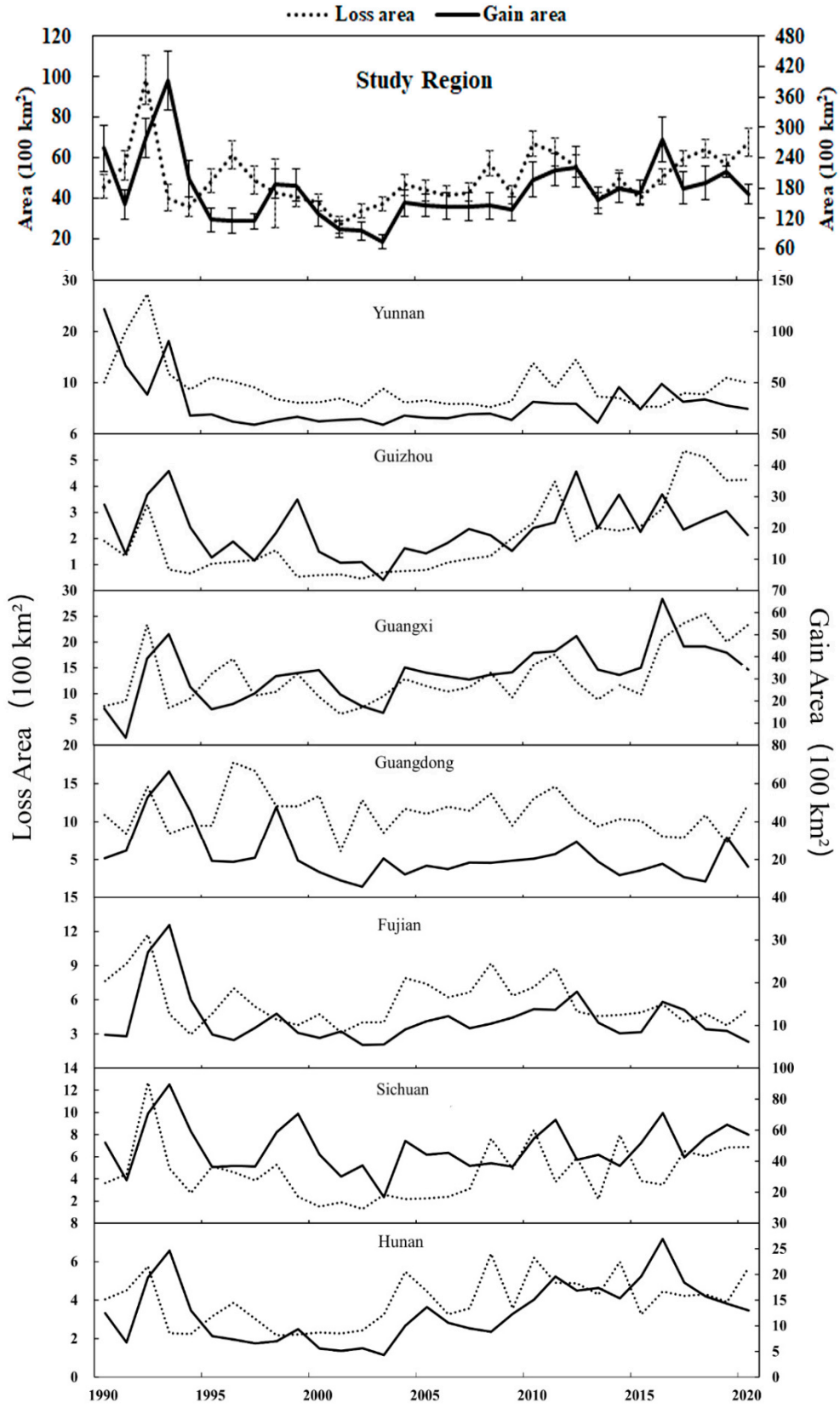

Figure 7. Forest loss and gain area (100 km^2) in the study region and different provinces during 1990–2020.

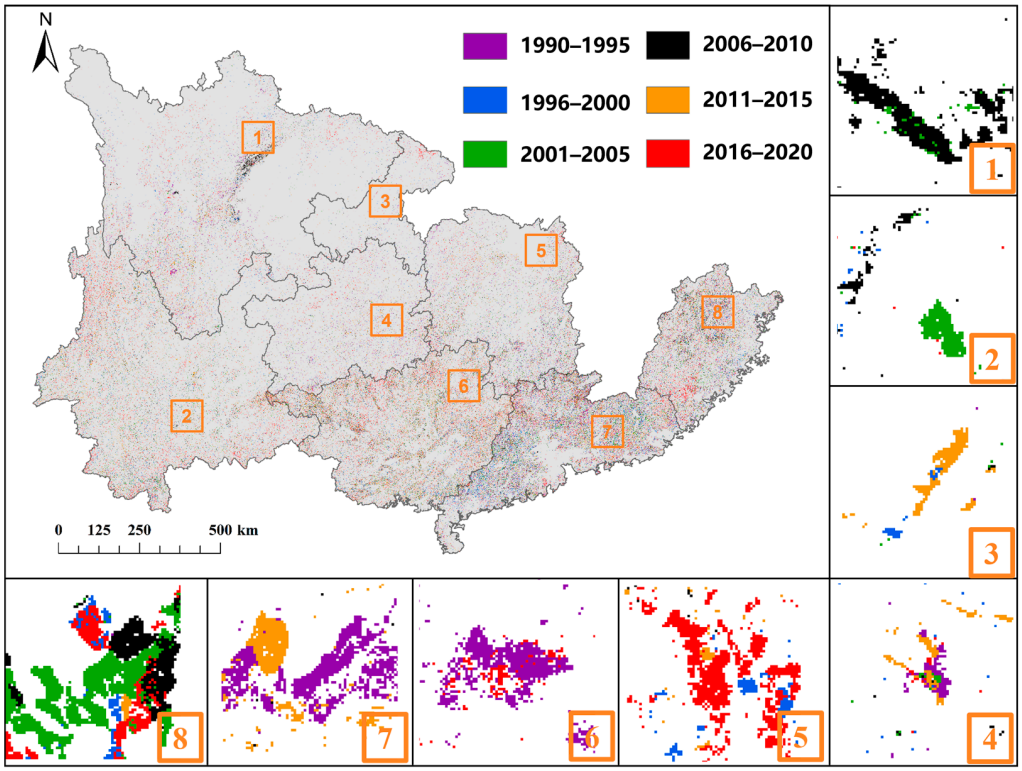

Figure 8. The spatial distribution of forest loss area and occurrence years in southern China. Note: the boxes from 1 to 8 are magnified areas (scaled to 1:10,000) to show clearer spatial patterns in forest loss area and years.

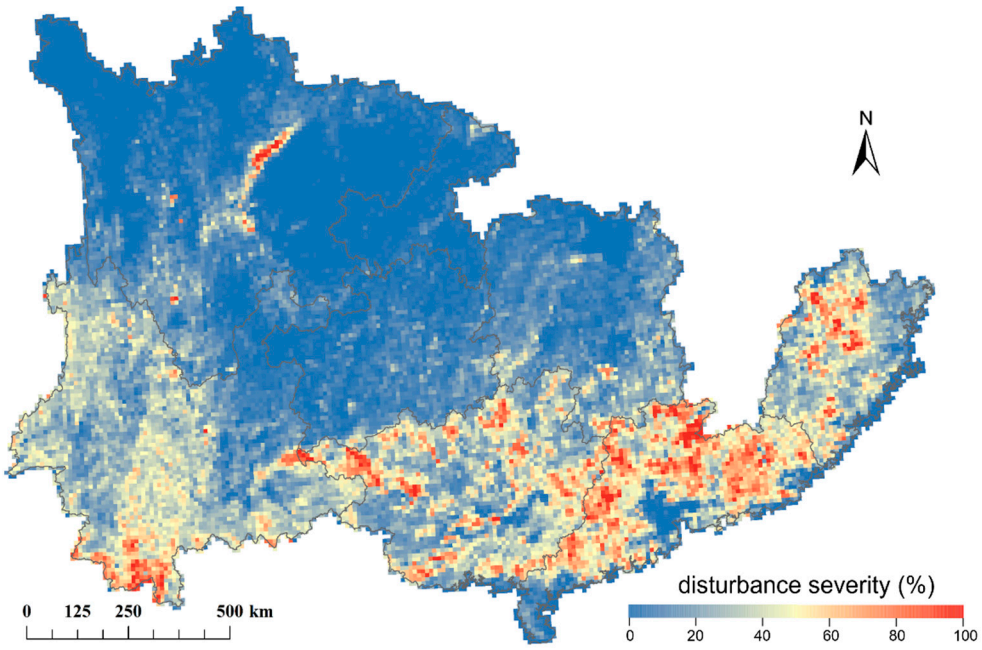

Figure 9. Forest disturbance severity (%) at 10 km spatial resolution in southern China.

4.4. Spatiotemporal Patterns in Forest Recovery Area

The total forest recovery area including both the gain after loss area and the afforested area (land use change) was 5.44×10^5 km^2 during 1990–2020, which accounted for 122.9% of the total forest area in 1990 (Figure 7). The mean annual forest gain area was $1.75 \times 10^4 \pm 0.29$ km^2. The mean CV was 16.51% due to the variations of the Max Segment from 4 to 10 and the Recovery Threshold from 0.25 to 1.0. The greatest and

smallest gain area occurred in 1993 (3.93×10^4 km^2) and 2003 (7429 km^2), respectively, which were one or two years after the greatest and smallest forest loss areas, respectively. The forest gain area also showed a decline from 1990–1993, and a significant increasing trend (slope = 302 km^2/year) from 1994 to 2020, though the interannual variations of the gain area were also very large (Figure 7).

At provincial levels, the Sichuan and Guangxi Provinces had the greatest gain area of 1.51×10^5 km^2 and 1.01×10^4 km^2, respectively, while the Hunan and Fujian Provinces had the smallest loss area of 3.53×10^4 km^2 and 3.92×10^4 km^2, respectively (Figure 7). The gain rates relative to the forest area in 1990 were the highest in Guangxi (193%) and Guizhou (271%) and the smallest in Hunan (58.1%) and Fujian (70.6%). All provinces showed the largest forest gain area in 1993. Similarly, the Guizhou, Guangxi, Hunan, and Sichuan Provinces showed significant increasing trends of 47.9 km^2/year, 96.7 km^2/year, 50.0 km^2/year, and 45.8 km^2/year, respectively, during 1994–2020, while other provinces showed no significant changing trends.

On a spatial scale, forest gain was more widely distributed than forest loss (Figure 10). Similar to the loss area, the forest gain areas were relatively more distributed in the forest edge areas. Most of the recovered forest areas were located in the loss area since forest recovery after loss is the main gain regime. From the magnified areas, we can also more clearly see that the forest loss area of each year is mainly concentrated as large patches since both forest recovery after loss and afforestation occurred with clustered patterns. Scaled-up to a 10 km spatial resolution, the forest gain fraction was further analyzed (Figure 11). The results indicated that central Sichuan, eastern Guangdong, southeastern Guizhou, and western Guangxi had the largest forest gain fractions which were higher than 80% at a 10 km spatial resolution.

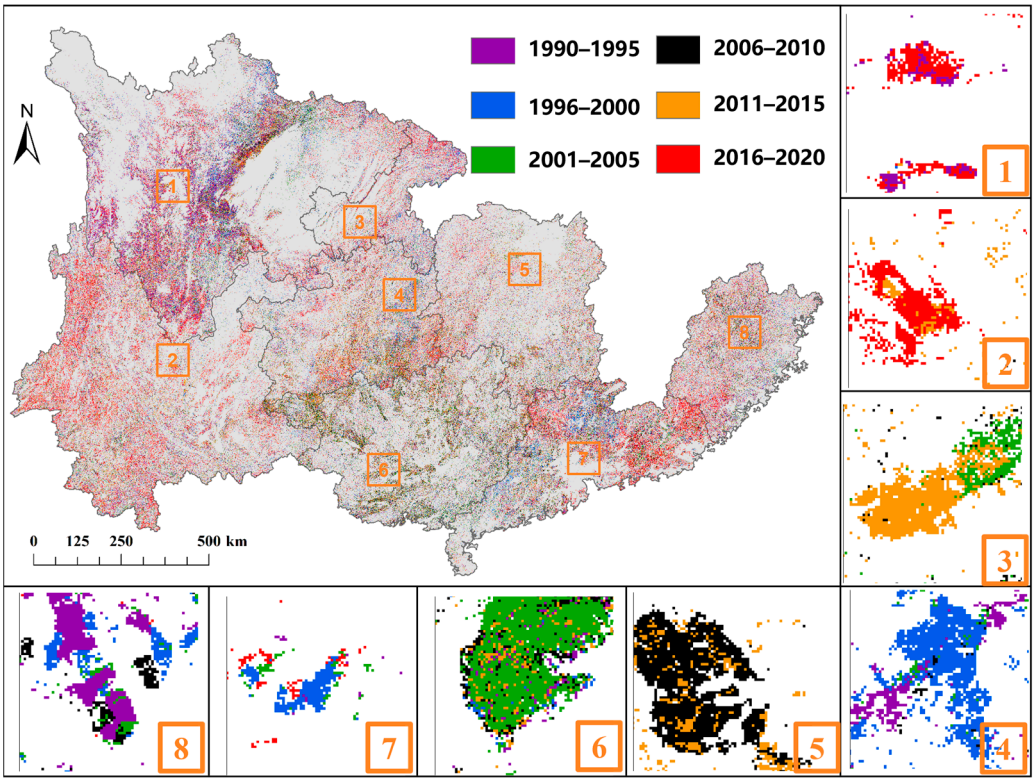

Figure 10. The spatial distribution of forest gain area and occurrence years in southern China. Note: the boxes from 1 to 8 are magnified areas (scaled to 1:10,000) to show clearer spatial patterns in forest gain area and years.

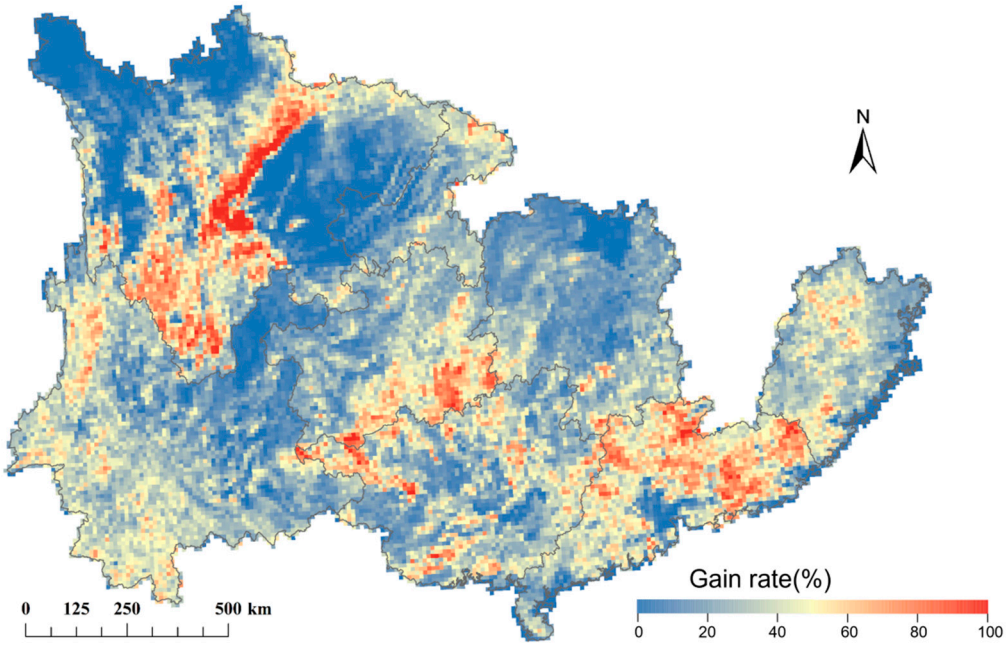

Figure 11. Fraction of forest gain area (%) at 10 km spatial resolution in southern China.

4.5. Forest Disturbance Frequency

With a detection window of 5 years, the frequency of forest disturbance during 1990–2020 was mainly dominated by one or two disturbance times (Figure 12). For the entire study region, about 88.5% of the forest loss areas were one-time disturbance and 11.50% of the forest loss areas were disturbed twice or more times. At a provincial scale, there were large differences in the proportions of disturbance frequency. Guangxi and Guangdong had the highest proportions of two or more times of forest disturbance, especially in the Guangxi Province where 21.05% of the forest loss areas have experienced two or more disturbance times, which is significantly higher than other provinces. The proportion of twice or more forest loss areas was the lowest in the Sichuan Province (5.32%).

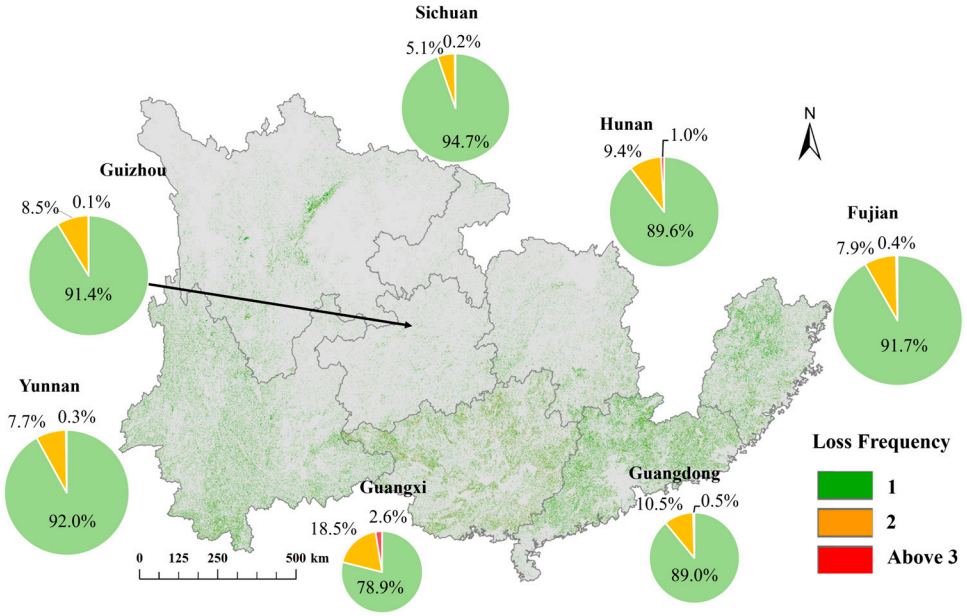

Figure 12. The forest disturbance frequency (times) and the area fraction in each province in southern China.

4.6. Overall Forest Dynamic in Southern China

By combining the detected forest disturbance and gain area, we further calculated the overall forest dynamic in southern China (Figure 13). During 1990–2020, the net forest loss area (land conversion from forest to other land covers) was 6.39×10^4 km^2. This accounted for about 42.1% of the total forest loss area and about 14.4% of the forest area in 1990. The forest gain after loss area was 8.94×10^4 km^2. The forest gain area was significantly greater than that of loss and thus the net gain area was 4.55×10^5 km^2, which accounted for 58.8% of the total forest gain area and about 72.2% of the forest area in 1990. The net gain forest area in each province matched well with the NFI statistical total afforestation area (Figure 13), indicating the adequate accuracy of our detected forest dynamic pattern in southern China.

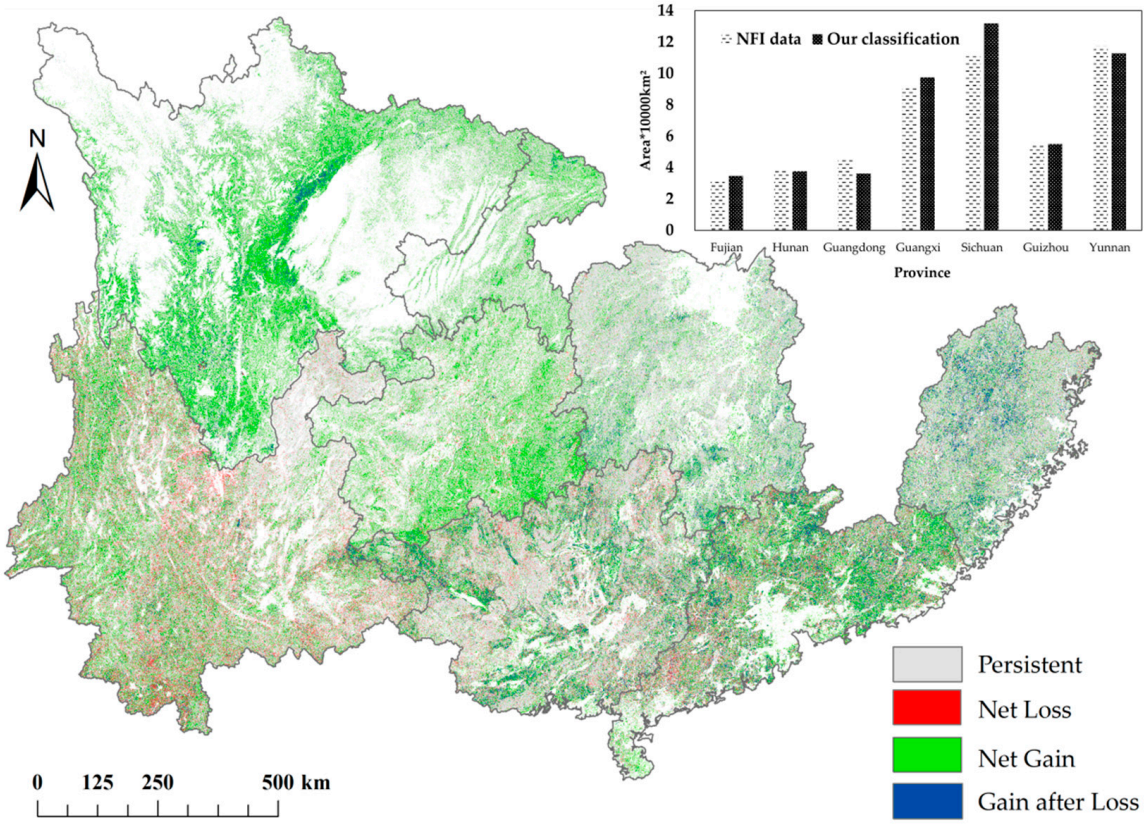

Figure 13. The overall forest dynamics including persistent, net loss, net gain, and gain after loss forest area in southern China during 1990–2020. Note: the top-right graph is the comparisons of the classified provincial net gain area with the National Forest Inventory (NFI) statistical afforestation area.

5. Discussion

5.1. Comparisons with Previous Studies

Although many studies have explored and concluded that the increasing forest area in southern China was the main contributor to the greening trend and carbon sink of China, these studies are mainly based on the statistical forest area data and the inversion using Vis [35,36]. At present, few accurate geospatial forest dynamic data in China can actually capture the spatial and temporal change patterns of the forest area due to the coarse spatial resolution or the lack of tracking of the forest disturbance and recovery dynamic information [37], for example, the widely used CLCD [28], NLCD, and China Annual Land Use/cover Dataset (CLUDA) [36], datasets which have all underestimated the forest gain during the past several decades. Our classified forest area and annual change patterns were comparable to the NFI statistical forest area at both regional and provincial scales (Figure 14). The comparisons indicated that our data were close to the NFI statistical data,

with a slight overestimation for forest area in the early period, primarily because many fractional (not standing-replacing) disturbance and recovery events were not detected in this study. However, the overall forest area and annual change rate detected using the default parameters were significantly lower than the NFI data, implying an underestimation of the forest area change. Our detected interannual forest loss area was further compared with the GFC forest loss product during 2001–2020 (Figure 15). A significant positive correlation ($R^2 = 0.67$; $p < 0.01$) existed between our results and the GFC product; however, the mean annual forest loss area of the GFC product was 4806 km^2, which was lower than our estimation (4931 km^2) during this period. This was mainly because the GFC product classified a lower forest loss area in the Sichuan and Yunnan Provinces.

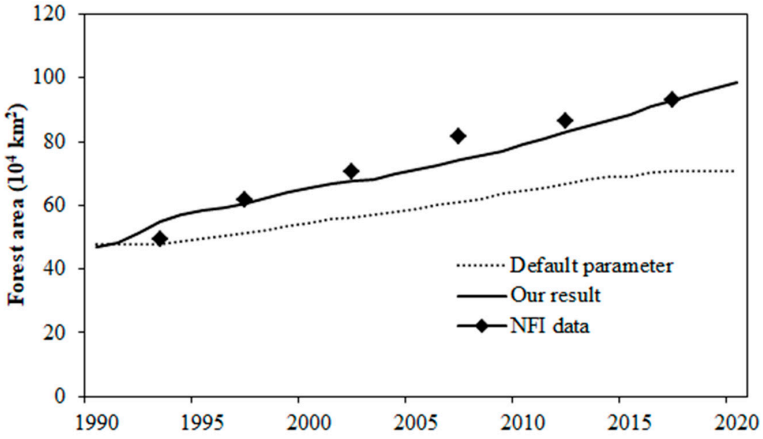

Figure 14. The comparison of the detected forest area during 1990–2020 using improved parameters (black line) and default parameters (dotted line) with the National Forest Inventory (NFI) statistical data (discrete points).

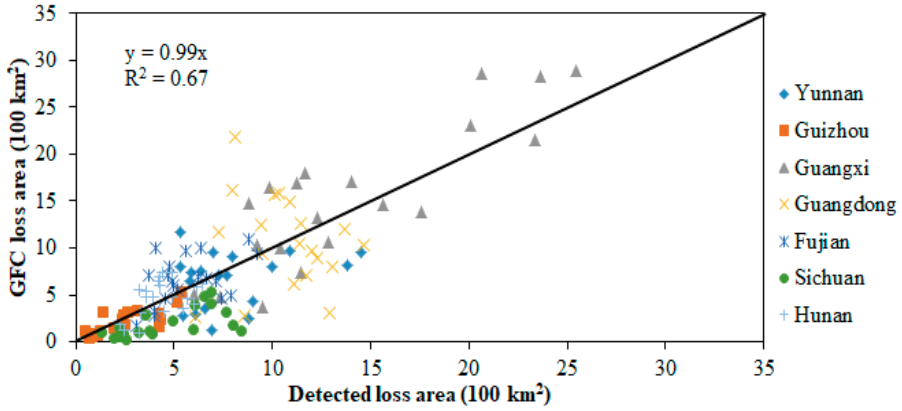

Figure 15. Comparisons of our detected annual forest loss area in different provinces with the global forest change (GFC) product [4].

Most of the previous studies based on the Landsat time-series imagery have found a significant decrease in the forest loss area during 1986–1990 [38,39], and we also found this phenomenon (Figure 7). Liu et al. [38] classified the patterns and trends of forest disturbances in China from 1986 to 2020 also using the coupled LandTrendr and RF methods, and concluded that there was no significant trend in the forest disturbance area in southern China. However, we found a significant increasing trend in the forest disturbance area in southern China during 2000–2020, which was primarily attributed to the significant increasing patterns in the Guangxi, Hunan, and Guizhou Provinces. In our previous study [39], we used the default LandTrendr parameters and also found no significant change trend in the forest loss area during 2000–2020.

5.2. Effectiveness of Improved Parameters on Forest Disturbance Detection

In recent years, many methods have been put forward to increase the LandTrendr accuracy for disturbance and recovery detection, such as the segment filtering method, input variables, the combination of multiple seasons, integrated classifiers, and the combination of multiple VIs [17,20–24]. However, few studies have specifically addressed the impacts of parameter values on the detection accuracy for spatiotempral patterns and the frequency of the forest loss area. Kennedy et al. [17] conducted a sensitivity analysis for the LandTrendr parameters and provided the parameter ranges. However, due to the difference in the climate, forest condition, and topography, the most suitable parameter sets should be calibrated for every piece of research using the LandTrendr algorithm. In a study of mapping mangrove dyanmics using LandTrendr, de Jong et al. [26] concluded that the success and robustness of the LandTrendr algorithm are controlled by NDVI Recovery Threshold values and the number of allowed breakpoints (max segment) in the time-series. They found that the effect of decreasing the Recovery Threshold from 0.5 (2 years) to 0.25 (4 years) has a deteriorating effect because mangrove areas that are visually identified as recovering are excluded, leading to the wrong identification of recovery timing. Qiu et al. [24] conducted a sensitivity analysis for different LandTrendr parameters for disturbance detection in China, and concluded that the optimal parameters for the Max Segments, Pval threshold, Recovery Threshold, and Best Model Proportion were 6, 0.01, 0.5, and 0.5, respectively, and the F1 score for these parameters did not differ very much except for the Max Segments and Recovery Threshold parameters. However, our study indicated that a Recovery Threshold of 0.25 was better for most provinces and 0.5 was better for the fastest recovery regions (Guangxi and Guangdong). Based on our evaluations, our optimized parameter values have higher accuracy for forest disturbance detection in southern China with faster recovery and a lower availability of noise- and cloud-free images. Most tree species in southern China need more than 4 years for the tree canopy to recover. In addition, the noise- and cloud-free images are less available in our study region due to high precipitaton. Therefore, the setting of too-short recovery years (e.g., 2 years) will result in the false identification of disturbance timing. Instead, the canopy of Eucalyptus trees can recover within 3 years in the Guangxi and Guangdong Provinces, and due to their larger planting areas and shorter rotation age, the Recovery Threshold parameter value of 0.5 was better for these two provinces. In a study of surface water dynamics using LandTrendr, Lothspeich, and Knight [40], we also found that a Recovery Threshold value of 0.25 was better for identifying water dynamics in Minnesota. Liu et al. [25] assessed the sensitivity of the Recovery Threshold parameters to the identification of fire disturbance and recovery in Australia and indicated that parameter values of both 0.5 and 0.25 were best for most ecosystems; they also implied that climate conditons affected the effectiveness of the parameter values.

The Max Segment parameter denotes the maximum number of segments to be fitted in the time-series. The greater Max Segment means more disturbance events can be detected within the study period. Generally, the higher Max Segmets can result in more disturbance times. The studies by de Jong et al. [26] and Kennedy et al. [17] found that the detection accuracy increased with the Max Segment numbers. But de Jong et al. [26] also argued that too many segments increased the chances of false-positives (the non-change area is wrongly identified as a disturbed area). In our study, we found that the best value of the Max Segment was eight, which is higher than the setting of Qiu et al. [24]. We found that this parameter is not very sensitive in the slower recovering region, while it is very sensitive in the faster recovering region, where more disturbance times can be identified after increasing the Max Segment parameter value. The study of Lothspeich and Knight [40] indicated that the Max Segment value of 11 was the best for identifying surface water dynamics; while Liu et al. [25] tested the sensitivity of a gradient of Max Segment parameters and indicated that either 6, 8, or 10 was good for identifying vegetation disturbances and recovery after fires in most of the study ecosystems.

The Magnitude Change Threshold was also found important to remove the false disturbance signal caused by variations of climate and low-intensity disturbances; therefore, it is especially useful in detecting stand-replacing disturbance events. Li et al. [41] found that different forest types and VIs should have different thresholds for the change magnitude ranging from 103 to 935, while our study found that this parameter should range from 200 to 280. We also found that the improved parameters of LandTrendr can not only increase the detection accuracy for the spatiotemporal patterns of forest loss and gain, but also increase the detected area of multiple disturbance events. Except for the above-mentioned parameters, other parameters in LandTrendr such as the Pval Threshold and Best Model Proportion can affect the performance of disturbance detection [17,25]; however, they are generally not very sensitive to variations within their value ranges.

According to the Chinese forestry operration standard (LY/T2908–2017), the rotation ages for the fast-growing and high-yield plantations generally range from 6 to 41 years in southern China. For example, the rotation ages for the main Chinese fir (*Cunninghamia lanceolata*) and masson pine (*Pinus massoniana* Lamb.) plantations are about 16–20 years and the Eucalyptus and poplar plantations are about 5–14 years in the Guangxi Province and the Guangdong Province. The timber production in the Guangxi Province accounts for over 40% of China's timber supply. Therefore, most timberlands in southern China experienced 1–5 times the disturbance during 1990–2020. Our results suggest that over 21.06% of the forest loss area has experienced disturbance events at least twice, implying the vital importance of the accurate detection of multiple disturbance events. Several previous studies [17,25,26] have also suggested that the parameter values could vary with the study regions. The LandTrendr algorithm is more widely applied recently due to the expanded users of the GEE platform. Therefore, we suggest that future applicators should also pay attention to optimizing the LandTrendr parameters over their study regions, in addition to improving the input variables, image quality, and trajectory fitting methods.

5.3. Effects of Forestry Policies and Projects

Some studies have indicated that the terrain, climate, and human activities were the major factors influencing the spatiotemporal distribution patterns of forest disturbance and recovery in China [19,24,38,42]. For most provinces in southern China, the policies could be the leading factor. For example, the income of the forestry sector in Guangdong and Guangxi accounts for a higher portion of the GDP due to the governmental policy for promoting the planting of commercial and economic forests. The terrain could be the second contributing factor since most disturbance events were caused by human activities, so the remote or inaccessible regions generally have lower disturbance rates, such as the Guizhou and Sichuan Provinces. In addition, the steep-slope and low-land-quality areas are often planned as protected regions and thus few disturbance events occur in these regions. In contrast, climate is less of an important factor since large-scale extreme climate events are relatively fewer in southern China.

Although there were some uncertainties caused by the quality of Landsat images, image preprocessing, changes detection algorithms, parameter values, and other sources, we can still find that the major forestry policies, regulations, and projects can significantly affect forest dynamics in southern China [43,44]. Since the 1980s, Chinese state authorities have successfully implemented a series of forestry policies and projects, as listed in Table A2. The highest forest loss area during 1990–1992 was the legacy effects from the "three determination" policy put forward in 1981 [45–48]. Under this policy, the forest right was transferred from nation-owned to the collective-owned (e.g., villages or administrative units) (Figure A2). The low forest loss area was mainly due to the legacy effects from the policy for enhancing forest management and the ban on indiscriminate tree felling in 1987, which reversed the effects from the "three determination" policy [49]. The trial implementation of the collective forest tenure reform (CFTR) policy in several provinces and the High-yield Plantation in Key Areas (FHPKA) policy in the Guangxi and Guangdong Provinces caused a continuous increase in the forest loss area. The mature forests owned

by private parties were harvested for profits under the impacts of CFTR. The increasing short rotation forest plantation area also caused an increasing harvesting area. The ful implementation of CFTR for all provinces in southern China further resulted in a long-term increase in the forest loss area during 2009–2017. The implementation of the National Forest Conservation Program (NFCP) in 2010, the public welfare forest conservation policy in 2013, the Reform of State-owned Forest Farms (RSFF) in 2015, and the stricter implementation of the forestry law in 2016 has caused a declining forest loss area since 2017. Van Den Hoek et al. [44] also applied the Tasseled Cap indices and a decision tree classifier and evaluated the effectiveness of NFCP and RSFF policies on forest cover in the Yunnan Province.

The interannual variation pattern of the forest recovery area generally showed a 1-to-3-year lag behind that of the forest loss area, since a large portion of forests was recovered from the forest loss areas. The forest conservation and protection policies can further enhance or counteract the variations [43,46]. For example, the policy for "Notice on Further Strengthening of Afforestation Progress" implemented in 1993 caused a peak forest gain area in 1994. The implementations of the Green for Grain Project (GFGP) policy in 1998 and the NFCP policy in 2010 resulted in a peak forest gain area in 1999 and 2011, respectively. In particular, the implementation of the second amendment of Forestry Law in 2016 resulted in a peak forest gain area in 2017.

6. Conclusions

The detection of forest disturbance and recovery was more challenging for southern China due to the complex climate, topography, forest conditions, fast-recovery of forests, and less availability of cloud-free Landsat images. Based on the plentiful sample plots, this study identified the most effective spectral information and optimized the parameters of the LandTrendr algorithm to achieve a more accurate detection of forest disturbance and recovery. The accuracy assessment against the plot data, statistical data, and other similar products at both temporal and spatial scales proved the good performance of our methods. The results indicated that the mean annual forest loss and gain area was 4981 km^2 and 1.75×10^4 km^2, respectively, and a large uncertainty can be caused by the parameter values. An increased trend of the forest gain and loss area was found during 2000–2020 for southern China, mainly owing to the significant increasing trends of the forest disturbance and recovery area in the Guizhou, Guangxi, and Hunan Provinces. The improved parameters help detect multiple forest disturbance events, implying that about 11.50% of the forest loss areas have been disturbed more than twice. The developed forest dynamic data based on the forest gain and loss area matched well with the provincial statistical data and thus can be effectively applied to assess forest resources, carbon cycling, and the impacts of forest policies and management. The temporal variations in the forest loss and gain area were mainly affected by the forestry policies, projects, and regulations. Compared to the default parameters, the overall accuracy of the optimized parameters can improve by 6.89% and 3.65%, respectively. In addition, the spatiotemporal patterns of the forest gain and loss area after parameter optimization matched better with the visually interpreted, the NFI, and the GFC datasets. All these implied that parameter optimization can greatly improve the forest disturbance and recovery detection performance in southern China. Certainly, due to the Landsat image quality, the preprocessing methods, the trajectory fitting and smoothing methods, the change detection algorithms and parameters, and the possible overfitting in RF, our detected forest loss and gain area could somehow deviate from the actual conditions; however, the uncertainty caused by these factors is difficult to fully quantify. Our study partially assessed the uncertainty resulting from LandTrend parameter values, and the results implied that the applications of LandTrendr in similar regions with fast-regrowing vegetation should pay more attention to improve the Max Segment and Recovery Threshold parameters, which will cause a lot of uncertainty, and their optimization can increase the accuracy for detecting multiple and lower-rate disturbance/recovery events. Considering that there are broader users of the LandTrendr algorithm and many previous studies generally applied the default parameters, we suggested that future users should

carefully calibrate the LandTrendr parameters during regional applications. Furthermore, the importance of input factors in the RF Classifier varies with the regions, so it is better to separately run the secondary RF classification at subregional scales.

Author Contributions: Conceptualization, Y.T. and G.C.; methodology, Y.T. and G.C.; validation, Y.T., H.J., Y.C. and K.L.; formal analysis, Y.T., K.L. and G.C.; data curation, Y.T., Y.C., H.J. and K.L.; writing—original draft preparation, Y.T.; writing—review and editing, G.C., Y.C. and K.L.; visualization, Y.T. and Y.C.; supervision, G.C.; project administration, G.C.; funding acquisition, G.C. All authors have read and agreed to the published version of the manuscript.

Funding: This work was funded by the China National Key Research and Development Program (Grant Number 2023YFE0105100), the Scientific Research Foundation of Zhejiang A&F University (Grant number 2034020080), and the Overseas Expertise Introduction Project for Discipline Innovation (111 Project; Grant number D18008).

Data Availability Statement: All data generated during this study are included in this article. The Landsat images are freely available at USGS Earth Explorer (https://earthexplorer.usgs.gov, accessed on 5 April 2024) or on the GEE platform (https://earthengine.google.com, accessed on 5 April 2024). The GFC products are freely available at https://glad.umd.edu/dataset (accessed on 5 April 2024) or on the GEE platform. The FROM-GLC10 dataset and associated sampling plot data are available at https://data-starcloud.pcl.ac.cn/zh (accessed on 5 April 2024). The NLCD dataset is available on the Resource and Environmental Science Data Platform (https://www.resdc.cn/, accessed on 5 April 2024). The CLCD dataset is available at https://doi.org/10.5281/zenodo.4417810 (accessed on 5 April 2024).

Conflicts of Interest: The authors declare no conflicts of interest.

Appendix A

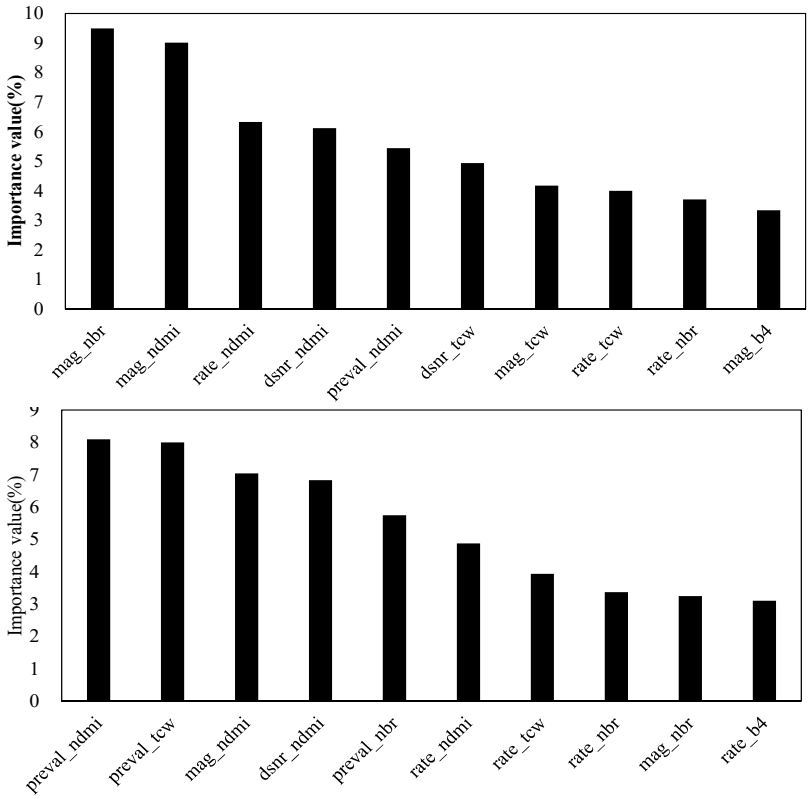

Figure A1. The ranking of relative importance (top 10) of different input variables in detecting forest disturbance and recovery in the RF classifier for Sichuan (**top**) and Guangxi (**bottom**) Province. Note: dur: duration of spectral change; preval: pre-disturbance spectral value; mag: spectral change magnitude; rate: spectral change rate; and dsnr: signal-to-noise ratio of spectral change.

Table A1. The sensitivity analysis for detected mean annual forest loss pixel numbers during 1990–2020 using different parameter values for Max Segment and Recovery Threshold in selected regions of all provinces. Note: the italic and bold numbers are values from the default and optimized parameter values, respectively.

Max Segment	Recovery Threshold			
	0.25	**0.5**	**0.75**	**1**
4	741	1213	1501	1919
6	1035	1829	2436	3113
8	**1229**	2318	3182	3946
10	1367	2640	3645	*4421*
12	1463	2845	5225	4683

Table A2. The sensitivity analysis for detected mean annual forest gain pixel numbers during 1990–2020 using different parameter values for Max Segment and Recovery Threshold in selected regions of all provinces. Note: the italic and bold numbers are values from the default and optimized parameter values, respectively.

Max Segment	Recovery Threshold			
	0.25	**0.5**	**0.75**	**1**
4	135	536	788	1292
6	239	964	1520	2379
8	**332**	1378	2187	3182
10	401	1652	2609	*3636*
12	466	1847	2848	3877

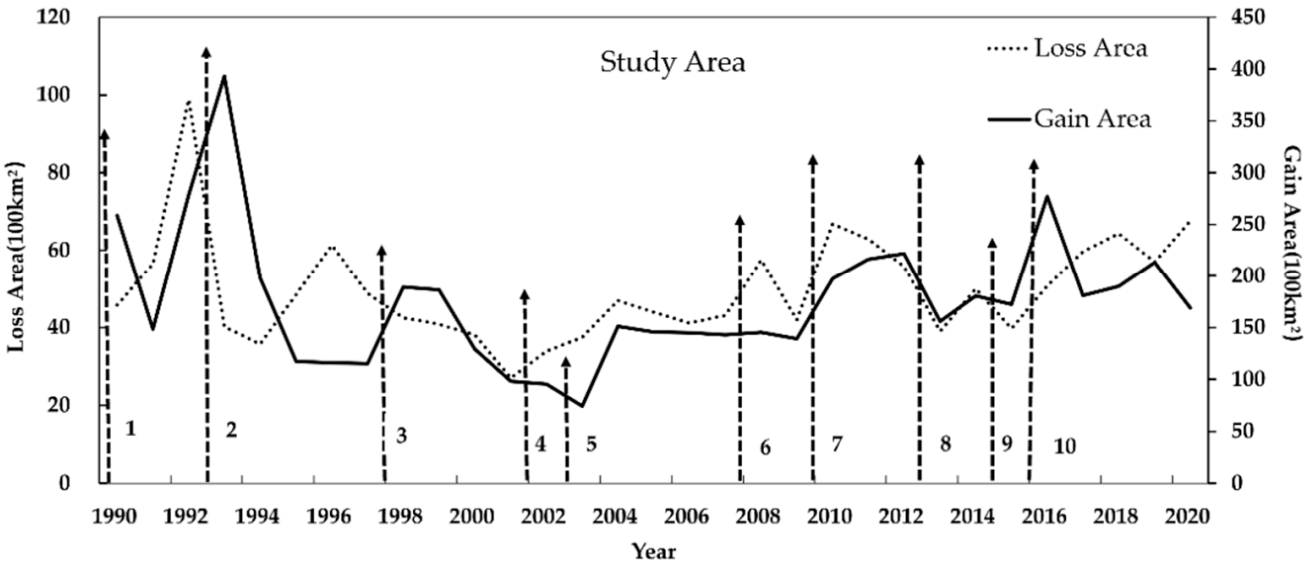

Figure A2. The implementation timeline of major forestry polices and their effects on the interannual variations of forest loss and gain area during 1990–2020. Note: the numbers along the dashed arrow lines are the policy symbols listed in Table A3.

Table A3. The major forestry policies and projects, and their implementation time and major effects.

Symbol	Time	Forestry Policies or Projects	Major Effects
1	1990	Outline of the National Afforestation Program for 1989–2000	Implementation of major afforestation projects across China
2	1993	Notice on Further Strengthening of Afforestation Progress	Push forward for the implementation of forestry projects
3	1998	Pilot implementation of the Green for Grain Project (GFGP)	Promote afforestation through land conversion from farmland
4	2002	Natural Forest Conservation Program (NFCP)	Promote the conservation of existing natural forest resources
4	2002	Project for Fast-growing and High-yield Plantation in Key Areas (FHPKA)	Shifting timberland base from the north to the south
5	2003	The trial time for the collective forest tenure reform (CFTR)	Forestland ownership change from collective to private rights in some cities in Sichuan and Fujian
6	2008	Ful implementation of CFTR	Realize the multiple functions of forests and increase household income
7	2010	The starting time for second stage of the NFCP	More strict implementation of the natural forest conservation policy
8	2013	The starting time for conserving the public welfare forests	To protect forests with important ecological functions
9	2015	Reform of state-owned forest farms (RSFF)	Forest farms shift from a profit-making agency to protection agency
10	2016	Regulations on the Implementation of the Forestry Law (Amendment 2016)	Protect forest resources and realize ecological civilization

References

1. McKinley, D.C.; Ryan, M.G.; Birdsey, R.A.; Giardina, C.P.; Harmon, M.E.; Heath, L.S.; Houghton, R.A.; Jackson, R.B.; Morrison, J.F.; Murray, B.C. A synthesis of current knowledge on forests and carbon storage in the united states. *Ecol. Appl.* **2011**, *21*, 1902–1924. [CrossRef] [PubMed]
2. Xu, W.; Jin, X.; Liu, J.; Yang, X.; Ren, J.; Zhou, Y. Analysis of spatio-temporal changes in forest biomass in china. *J. For. Res.* **2022**, *33*, 261–278. [CrossRef]
3. Pugh, T.A.; Arneth, A.; Kautz, M.; Poulter, B.; Smith, B. Important role of forest disturbances in the global biomass turnover and carbon sinks. *Nat. Geosci.* **2019**, *12*, 730–735. [CrossRef] [PubMed]
4. Hansen, M.C.; Potapov, P.V.; Moore, R.; Hancher, M.; Turubanova, S.A.; Tyukavina, A.; Thau, D.; Stehman, S.V.; Goetz, S.J.; Loveland, T.R.; et al. High-resolution global maps of 21st-century forest cover change. *Science* **2013**, *342*, 850–853. [CrossRef] [PubMed]
5. Song, X.P.; Hansen, M.C.; Stehman, S.V.; Potapov, P.V.; Tyukavina, A.; Vermote, E.F.; Townshend, J.R. Global land change from 1982 to 2016. *Nature* **2018**, *560*, 639–643. [CrossRef] [PubMed]
6. Turner, M.G. Disturbance and landscape dynamics in a changing world. *Ecology* **2010**, *91*, 2833–2849. [CrossRef] [PubMed]
7. Xiao, H.; Zhang, X.; Yan, M.; Zhang, L.; Wang, H.; Ma, Y.; Liu, J. The temporal-based forest disturbance monitoring analysis: A case study of nature reserves of hainan island of china from 1987 to 2020. *Front. Environ. Sci.* **2022**, *10*, 891752. [CrossRef]
8. Tollerud, H.J.; Zhu, Z.; Smith, K.; Wellington, D.F.; Hussain, R.A.; Viola, D. Toward consistent change detection across irregular remote sensing time series observations. *Remote Sens. Environ.* **2023**, *285*, 113372. [CrossRef]
9. Serneels, S.; Said, M.Y.; Lambin, E.F. Land cover changes around a major east african wildlife reserve: The mara ecosystem (kenya). *Int. J. Remote Sens.* **2001**, *22*, 3397–3420. [CrossRef]
10. Lu, D.; Mausel, P.; Brondizio, E.; Moran, E. Change detection techniques. *Int. J. Remote Sens.* **2004**, *25*, 2365–2401. [CrossRef]
11. Banskota, A.; Kayastha, N.; Falkowski, M.J.; Wulder, M.A.; Froese, R.E.; White, J.C. Forest monitoring using landsat time series data: A review. *Can. J. Remote Sens.* **2014**, *40*, 362–384. [CrossRef]
12. Zhu, Z. Change detection using landsat time series: A review of frequencies, preprocessing, algorithms, and applications. *ISPRS J. Photogramm. Remote Sens.* **2017**, *130*, 370–384. [CrossRef]
13. Huang, C.; Goward, S.N.; Schleeweis, K.; Thomas, N.; Masek, J.G.; Zhu, Z. Dynamics of national forests assessed using the landsat record: Case studies in eastern united states. *Remote Sens. Environ.* **2009**, *113*, 1430–1442. [CrossRef]

14. Verbesselt, J.; Hyndman, R.; Newnham, G.; Culvenor, D. Detecting trend and seasonal changes in satellite image time series. *Remote Sens. Environ.* **2010**, *114*, 106–115. [CrossRef]
15. Brooks, E.B.; Wynne, R.H.; Thomas, V.A.; Blinn, C.E.; Coulston, J.W. On-the-fly massively multitemporal change detection using statistical quality control charts and landsat data. *IEEE Trans. Geosci. Remote Sens.* **2013**, *52*, 3316–3332. [CrossRef]
16. Zhu, Z.; Woodcock, C.E. Continuous change detection and classification of land cover using all available landsat data. *Remote Sens. Environ.* **2014**, *144*, 152–171. [CrossRef]
17. Kennedy, R.; Yang, Z.; Cohen, W. Detecting trends in forest disturbance and recovery using yearly landsat time series: 1. Landtrendr—Temporal segmentation algorithms. *Remote Sens. Environ.* **2010**, *114*, 2897–2910. [CrossRef]
18. Pasquarella, V.J.; Arévalo, P.; Bratley, K.H.; Bullock, E.L.; Gorelick, N.; Yang, Z.; Kennedy, R.E. Demystifying landtrendr and ccdc temporal segmentation. *Int. J. Appl. Earth Obs.* **2022**, *110*, 102806–102818. [CrossRef]
19. Ding, N.; Li, M. Mapping forest abrupt disturbance events in southeastern china—Comparisons and tradeoffs of landsat time series analysis algorithms. *Remote Sens.* **2023**, *15*, 5408.
20. Kennedy, R.; Cohen, W.; Schroeder, T. Trajectory-based change detection for automated characterization of forest disturbance dynamics. *Remote Sens. Environ.* **2007**, *110*, 370–386. [CrossRef]
21. Kennedy, R.; Yang, Z.; Gorelick, N.; Braaten, J.; Cavalcante, L.; Cohen, W.; Healey, S. Implementation of the landtrendr algorithm on google earth engine. *Remote Sens.* **2018**, *10*, 691. [CrossRef]
22. Cohen, W.; Healey, S.; Yang, Z.; Zhu, Z.; Gorelick, N. Diversity of algorithm and spectral band inputs improves landsat monitoring of forest disturbance. *Remote Sens.* **2020**, *12*, 1673. [CrossRef]
23. Cohen, W.; Yang, Z.; Healey, S.; Kennedy, R.; Gorelick, N. A landtrendr multispectral ensemble for forest disturbance detection. *Remote Sens. Environ.* **2018**, *205*, 131–140. [CrossRef]
24. Qiu, D.; Liang, Y.; Shang, R.; Chen, J.M. Improving landtrendr forest disturbance mapping in china using multi-season observations and multispectral indices. *Remote Sens.* **2023**, *15*, 2381. [CrossRef]
25. Liu, W.; Guan, H.; Hesp, P.A.; Batelaan, O. Remote sensing delineation of wildfire spatial extents and post-fire recovery along a semi-arid climate gradient. *Ecol. Inform.* **2023**, *78*, 102304. [CrossRef]
26. de Jong, S.M.; Shen, Y.; de Vries, J.; Bijnaar, G.; van Maanen, B.; Augustinus, P.; Verweij, P. Mapping mangrove dynamics and colonization patterns at the suriname coast using historic satellite data and the landtrendr algorithm. *Int. J. Appl. Earth Obs. Geoinf.* **2021**, *97*, 102293. [CrossRef]
27. Li, C.; Gong, P.; Wang, J.; Zhu, Z.; Biging, G.S.; Yuan, C.; Hu, T.; Zhang, H.; Wang, Q.; Li, X.; et al. The first all-season sample set for mapping global land cover with landsat-8 data. *Sci. Bull.* **2017**, *62*, 508–515. [CrossRef] [PubMed]
28. Yang, J.; Huang, X. The 30m annual land cover dataset and its dynamics in china from 1990 to 2019. *Earth Syst. Sci. Data* **2021**, *13*, 3907–3925. [CrossRef]
29. Liu, J.; Kuang, W.; Zhang, Z.; Xu, X.; Qin, Y.; Ning, J.; Zhou, W.; Zhang, S.; Li, R.; Yan, C. Spatiotemporal characteristics, patterns, and causes of land-use changes in china since the late 1980s. *J. Geogr. Sci.* **2014**, *24*, 195–210. [CrossRef]
30. Gong, P.; Liu, H.; Zhang, M.; Li, C.; Wang, J.; Huang, H.; Clinton, N.; Ji, L.; Li, W.; Bai, Y.; et al. Stable classification with limited sample: Transferring a 30-m resolution sample set collected in 2015 to mapping 10-m resolution global land cover in 2017. *Sci. Bull.* **2019**, *64*, 370–373. [CrossRef]
31. Kennedy, R.; Yang, Z.; Braaten, J.; Copass, C.; Antonova, N.; Jordan, C.; Nelson, P. Attribution of disturbance change agent from landsat time-series in support of habitat monitoring in the puget sound region, USA. *Remote Sens. Environ.* **2015**, *166*, 271–285. [CrossRef]
32. Toledo, M.; Poorter, L.; Peña-Claros, M.; Alarcón, A.; Balcázar, J.; Leaño, C.; Licona, J.C.; Llanque, O.; Vroomans, V.; Zuidema, P. Climate is a stronger driver of tree and forest growth rates than soil and disturbance. *J. Ecol.* **2011**, *99*, 254–264. [CrossRef]
33. Cutler, D.R.; Edwards, T.C.; Beard, K.H.; Cutler, A.; Hess, K.T.; Gibson, J.; Lawler, J.J. Random forests for classification in ecology. *Ecology* **2007**, *88*, 2783–2792. [CrossRef] [PubMed]
34. Stehman, S. Selecting and interpreting measures of thematic classification accuracy. *Remote Sens. Environ.* **1997**, *62*, 77–89. [CrossRef]
35. Zhu, Z.C.; Piao, S.L.; Myneni, R.B.; Huang, M.T.; Zeng, Z.Z.; Canadell, J.G.; Ciais, P.; Sitch, S.; Friedlingstein, P.; Arneth, A.; et al. Greening of the earth and its drivers. *Nat. Clim. Change* **2016**, *6*, 791–795. [CrossRef]
36. Xu, Y.; Yu, L.; Peng, D.; Zhao, J.; Cheng, Y.; Liu, X.; Li, W.; Meng, R.; Xu, X.; Gong, P. Annual 30-m land use/land cover maps of china for 1980–2015 from the integration of avhrr, modis and landsat data using the bfast algorithm. *Sci. China Earth Sci.* **2020**, *63*, 1390–1407. [CrossRef]
37. Xia, X.; Xia, X.; Chen, X.; Fan, L.; Liu, S.; Qin, Y.; Qin, Z.; Xiao, X.; Xu, W.; Yue, C.; et al. Reconstructing long-term forest cover in china by fusing national forest inventory and 20 land use and land cover data sets. *J. Geophys. Res. Biogeosci.* **2023**, *128*, e2022JG007101.
38. Liu, Z.; Wang, W.J.; Ballantyne, A.; He, H.S.; Wang, X.; Liu, S.; Ciais, P.; Wimberly, M.C.; Piao, S.; Yu, K.; et al. Forest disturbance decreased in china from 1986 to 2020 despite regional variations. *Commun. Earth Environ.* **2023**, *4*, 15. [CrossRef]
39. Shen, J.; Chen, G.; Hua, J.; Huang, S.H.; Ma, J. Contrasting forest loss and gain patterns in subtropical china detected using an integrated landtrendr and machine-learning method. *Remote Sens.* **2022**, *14*, 3238. [CrossRef]
40. Lothspeich, A.C.; Knight, J.F. The applicability of landtrendr to surface water dynamics: A case study of minnesota from 1984 to 2019 using google earth engine. *Remote Sens.* **2022**, *14*, 2662. [CrossRef]

41. Li, Y.; Xu, X.; Wu, Z.; Fan, H.; Tong, X.; Liu, J. A forest type-specific threshold method for improving forest disturbance and agent attribution mapping. *GIScience Remote Sens.* **2022**, *59*, 1624–1642. [CrossRef]
42. Hua, J.; Chen, G.; Yu, L.; Ye, Q.; Jiao, H.; Luo, X. Improved mapping of long-term forest disturbance and recovery dynamics in the subtropical china using all available landsat time-series imagery on google earth engine platform. *IEEE J. Sel. Top. Appl. Earth Obs. Remote Sens.* **2021**, *14*, 2754–2768. [CrossRef]
43. Wang, G.; Innes, J.L.; Lei, J.; Dai, S.; Wu, S.W. China's forestry reforms. *Science* **2007**, *318*, 1556–1557. [CrossRef] [PubMed]
44. Van Den Hoek, J.; Ozdogan, M.; Burnicki, A.; Zhu, A.X. Evaluating forest policy implementation effectiveness with a cross-scale remote sensing analysis in a priority conservation area of southwest china. *Appl. Geogr.* **2014**, *47*, 177–189. [CrossRef]
45. Yin, R.; Newman, D. Impacts of rural reform: The case of the chinese forest sector. *Environ. Dev. Econ.* **1997**, *2*, 289–303. [CrossRef]
46. Zhang, D. China's forest expansion in the last three plus decades: Why and how? *For. Policy Econ.* **2019**, *98*, 75–81. [CrossRef]
47. Hyde, W.F.; Yin, R.S. 40 years of china's forest reforms: Summary and outlook. *For. Policy Econ.* **2019**, *98*, 90–95. [CrossRef]
48. Zhang, X.; Wu, S.; Ning, Y. An analysis on china's institutional change of collective forest tenure system and its economic motivation. *J. Beijing For. Univ. (Soc. Sci.)* **2015**, *14*, 57–63.
49. Liu, C.; Wang, S.; Liu, H.; Zhu, W. Why did the 1980s' reform of collective forestland tenure in southern china fail? *For. Policy Econ.* **2017**, *83*, 131–141. [CrossRef]